Electronic Research Archive

http://www.aimspress.com/journal/era

ERA, 34(11): 8689–8718.
DOI: 10.3934/era.2026366
Received: 16 July 2026
Revised: 29 August 2026
Accepted: 07 September 2026
Published: 10 October 2026

Research article

Mean-square exponential ultimate boundedness of networked control systems with packet-loss-adaptive event triggering and scale-normalized encoding

Xiuguang Ding*, Yuhao Zhang, Jiankai Xue and Jianping Zhou

School of Computer Science and Technology, Anhui University of Technology, Ma'anshan 243032, China

* **Correspondence:** Email: dingxg@ahut.edu.cn.

Abstract: This paper investigates mean-square exponential ultimate boundedness (MSEUB) for bandwidth-limited networked control systems subject to Bernoulli packet losses and finite-bit communication. A packet-loss-adaptive, event-triggered mechanism updates the triggering threshold according to the number of consecutive packet losses. It also enforces a positive minimum inter-event time. A scale-normalized encoding–decoding method is then constructed for finite-bit output transmission. Before quantization, the sampled output is normalized using a scale retained locally at the field-side node. The finite-bit index vector representing the normalized output is transmitted through the sensor-to-controller channel subject to packet losses. A stochastic closed-loop model is established by decomposing the Bernoulli packet-reception variable into its mean and zero-mean fluctuation. Tractable conditions are then derived to ensure MSEUB under Bernoulli packet losses and finite-bit reconstruction errors. Finally, numerical simulations illustrate the closed-loop and communication performance of the proposed design.

Keywords: mean-square exponential ultimate boundedness; networked control systems; event-triggered control; finite-bit encoding; packet losses

1. Introduction

In recent years, networked control systems (NCSes) have been applied to autonomous aerial vehicles [1], wireless industrial automation [2], and multi-agent consensus control [3]. Their sensing, communication, computation, and actuation functions are typically distributed across interconnected nodes [4]. In edge-enabled industrial systems, communication scheduling and control can be jointly designed [5]. Sensor nodes acquire plant outputs, controllers compute control commands, and actuators apply the corresponding control inputs to the plant [6]. End–edge collaboration further

places control-related processing near field devices [7]. Computation and compression latencies can influence end-to-end timing [8]. Practical NCSes additionally face resource-constrained edge devices [9] and limited communication bandwidth [10]. Networked information exchange can also be affected by communication latency [11]. Packet losses remain an important communication constraint in closed-loop NCS operation [12, 13]. Communication delays and sampling constraints can further affect closed-loop stability [14, 15]. Sampled-data modeling captures the interaction between continuous-time plant evolution and discrete controller updates. Within this framework, stability analysis and controller synthesis based on linear matrix inequalities (LMIs) provide tractable tools for closed-loop design [16, 17]. These considerations motivate the joint treatment of transmission scheduling and finite-bit output representation.

In bandwidth-limited NCSes, the communication rate is an important metric for resource planning [18]. Periodic transmission of all sampled information may therefore be inefficient, especially when the measured output changes only slightly. To reduce unnecessary transmissions, various communication scheduling strategies, including the stochastic communication protocol (SCP), have been investigated [19, 20]. Among them, event-triggered mechanisms provide nonperiodic transmission by releasing information or control actions only when prescribed conditions are satisfied [21, 22]. Such mechanisms can reduce communication and computation burdens while maintaining closed-loop stability. Adaptive and dynamic event-triggered strategies have also been studied for learning-based and data-driven control [23, 24]. Event-triggered methods have further considered asymptotic tracking [25]. Related designs have addressed security compensation and synchronization under different triggering structures [26, 27]. Fixed-time regulation with input nonlinearities has also been investigated using dynamic event-triggered designs [28]. Practical network constraints have also received considerable attention. Sun et al. [29] developed a threshold-dependent secure event-triggered control mechanism (TDSETCM) under denial-of-service (DoS) attacks. Wu et al. [30] investigated a dynamic periodic event-triggered control mechanism (DPETCM) for nonlinear cyber–physical systems under denial-of-service (DoS) attacks. Zeng et al. [31] considered robust tracking control under bounded packet dropouts and external disturbances. Wang et al. [32] developed looped-functional-based output-feedback conditions for aperiodic sampled-data systems. Together, these studies provide a basis for communication-efficient control and stability analysis under unreliable and nonperiodic network updates.

Communication usage in NCSes is determined jointly by transmission instants and the finite-bit representation of feedback information. Quantized communication has been investigated for event-triggered consensus under asynchronous DoS attacks [33] and resilient control of uncertain NCSes [34]. Finite-bit feedback can also be corrupted by bit-level channel errors, which may degrade the information available for closed-loop control [35]. Various encoding–decoding constructions have also been investigated in quantized control [36, 37]. Although such methods reduce transmitted payloads, finite-bit reconstruction errors enter the control loop. The integration of encoding–decoding mechanisms with closed-loop control has also been investigated. Liu et al. [38] studied observer-based control of networked periodic piecewise systems using an encoding–decoding mechanism. Wakaiki [39] developed a dynamic quantization with a zoom-parameter encoding–decoding method (DQZPEDM) for systems subject to quantization and packet loss. Zhou et al. [40] investigated robust finite-time stabilization using a limited static state-quantization encoding–decoding method (LSSQEDM). This study further characterized the effects of finite

quantization levels on closed-loop performance. Together, these studies addressed finite-bit encoding–decoding and quantization under different network constraints.

Although the above studies have advanced event-triggered transmission, finite-bit encoding–decoding, and quantized control, two issues remain in bandwidth-limited NCSes. First, many existing triggering rules determine transmission instants according to state deviations, output variations, or prescribed threshold parameters. These rules mainly evaluate whether the newly sampled signal differs sufficiently from the last transmitted signal. However, packet losses may prevent a triggered packet from being received by the controller, making the corresponding feedback update unavailable. Consequently, the controller-side update rate depends on the triggering error and packet-loss history. If this loss history is not reflected in the triggering threshold, the triggering rule may not promote timely transmission attempts after repeated packet losses. Second, finite-bit encoding–decoding schemes can reduce communication usage. However, the output magnitude may vary over time, whereas only a limited number of bits are available for transmission. Without appropriate scale normalization, balancing output-amplitude coverage and reconstruction accuracy remains difficult.

To address these issues, this paper develops an event-triggered control framework for bandwidth-limited linear NCSes. Its main contributions are summarized as follows. First, a packet-loss-adaptive event-triggered mechanism (PLAETM) is proposed to adjust the triggering threshold according to consecutive packet losses, thereby promoting subsequent transmission attempts after unsuccessful receptions. Numerical comparisons with adapted implementations of SCP [19], TDSETCM [29], and DPETCM [30] show that PLAETM reduces sensor-to-controller transmission attempts relative to SCP and TDSETCM while maintaining comparable closed-loop regulation under the stated parameter settings. Second, a scale-normalized encoding–decoding method (SNEDM) is developed to represent sampled outputs using fixed-length finite-bit indices without prescribing a raw-output quantization range or recursively updating a dynamic range. Numerical comparisons with LSSQEDM [40] and DQZPEDM [39] show that SNEDM achieves the lowest integral reconstruction error among the compared methods under the common trajectory and bit-length settings considered in the numerical study while avoiding overflow and requiring neither a prescribed raw-output range nor recursive dynamic zooming. Third, a stochastic closed-loop model is established to capture the coupled effects of packet-loss-dependent triggering, packet reception, and finite-bit reconstruction errors. Sufficient conditions for mean-square exponential ultimate boundedness (MSEUB) and a tractable controller-design condition are then derived.

Notations: Expectations and probabilities are denoted by $\mathbb{E}\{\cdot\}$ and $\mathbb{P}\{\cdot\}$, respectively. The integers n_x, n_u, and n_y denote the dimensions of the state, input, and output. The symbols $\mathbb{R}^n$ and $\mathbb{R}^{n\times r}$ denote the corresponding real vector and matrix spaces. The operator $\mathrm{diag}\{\cdot\}$ constructs a block-diagonal matrix. For a square matrix $\mathbf{G}$, $\mathrm{He}(\mathbf{G}) = \mathbf{G} + \mathbf{G}^{\mathrm{T}}$. The identity matrix of dimension n is denoted by $\mathbf{I}_n$; its subscript is omitted when the dimension is clear. The notation $\|\cdot\|_p$ denotes the vector p-norm for $p \in \{1, 2, \infty\}$, with $\|\cdot\| = \|\cdot\|_2$. For a real symmetric matrix $\mathbf{G}$, $\lambda_{\min}(\mathbf{G})$ and $\lambda_{\max}(\mathbf{G})$ denote its minimum and maximum eigenvalues. The symbol $*$ represents a transposed symmetric block in a symmetric matrix.

2. Preliminaries

This section presents the considered bandwidth-limited NCS and its signal flow, as illustrated in Figure 1. The sensor samples the plant output, and PLAETM determines whether the current sample is released. Once an event is generated, the encoder normalizes and quantizes the sampled output. Only the resulting finite-bit index vector is transmitted through the sensor-to-controller channel subject to packet losses. Decoder 1 reconstructs the normalized output for control computation, and Decoder 2 recovers the physical control input applied to the plant. The plant model, PLAETM, and SNEDM are formulated in the following subsections.

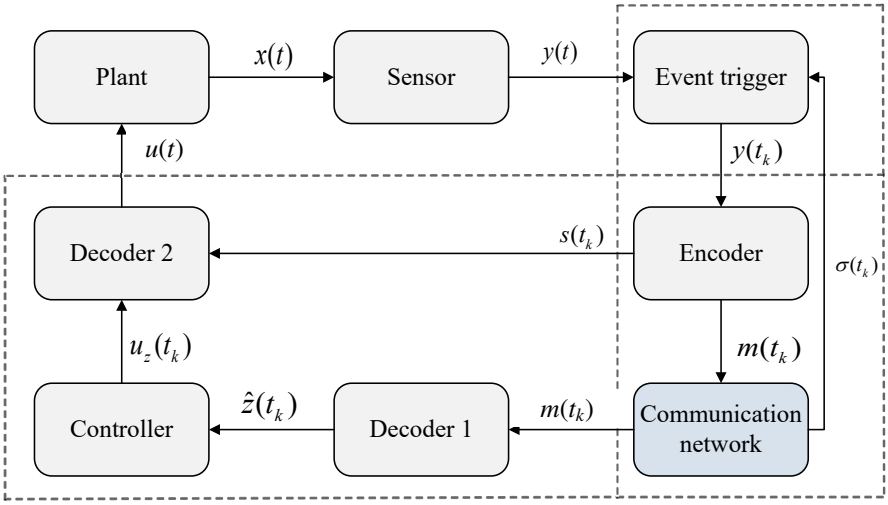


Figure 1. Architecture of the proposed PLAETM–SNEDM framework.

2.1. System model

The plant dynamics are described by the continuous-time linear plant

$$\dot{x}(t) = \mathbf{A}x(t) + \mathbf{B}u(t),\ y(t) = \mathbf{C}x(t), \tag{2.1}$$

where $x(t) \in \mathbb{R}^{n_x}$, $u(t) \in \mathbb{R}^{n_u}$, and $y(t) \in \mathbb{R}^{n_y}$ represent the plant state, the actuator input, and the sensor-side measured output. The matrices $\mathbf{A} \in \mathbb{R}^{n_x \times n_x}$, $\mathbf{B} \in \mathbb{R}^{n_x \times n_u}$, and $\mathbf{C} \in \mathbb{R}^{n_y \times n_x}$ are known constants.

2.2. PLAETM

This subsection introduces the PLAETM for bandwidth-limited NCSes with random packet losses. PLAETM releases a sampled output only when the triggering condition is satisfied. A minimum inter-event time is imposed to avoid arbitrarily dense transmissions, and the triggering threshold is adjusted according to the number of consecutive packet losses. Consequently, repeated transmission failures reduce the threshold for the next triggering decision and promote a new transmission attempt.

The triggering instants are denoted by

$$0 = t_0 < t_1 < \cdots < t_k < \cdots$$

and satisfy

$$t_{k+1} - t_k \geq T_{\min}, \ \lim_{k\to\infty} t_k = \infty, \tag{2.2}$$

where $T_{\min} > 0$ denotes the minimum interevent time. When an event occurs at t_k, the sampled output $y(t_k)$ is released for finite-bit encoding and transmission to the edge controller through the sensor-to-controller channel subject to packet losses.

The packet-reception status at t_k is represented by $\sigma(t_k) \in \{0, 1\}$, where $\sigma(t_k) = 1$ denotes successful reception, and $\sigma(t_k) = 0$ denotes packet loss. The sequence $\{\sigma(t_k)\}$ is modeled as independent Bernoulli trials satisfying

$$\mathbb{P}\{\sigma(t_k) = 1\} = p_s, \ \mathbb{P}\{\sigma(t_k) = 0\} = p_{\text{loss}} = 1 - p_s,$$

where $p_s \in (0, 1]$ denotes the packet-reception probability, and $p_{\text{loss}} = 1 - p_s$ denotes the packet-loss probability. The consecutive-loss counter is updated according to

$$r_{k+1} = \begin{cases} 0, & \sigma(t_k) = 1, \\ r_k + 1, & \sigma(t_k) = 0. \end{cases} \tag{2.3}$$

The packet-reception outcome associated with each triggered transmission is determined by the communication interface and made available to the field-side triggering unit through the reception-status feedback path shown in Figure 1. A successfully delivered packet is decoded and used for the control update at t_k, as represented by the delay-free model. For the causal update of PLAETM, the reception status becomes available before the earliest admissible next triggering test at $t_k + T_{\min}$. Upon obtaining $\sigma(t_k)$, the consecutive-loss counter r_{k+1} is first updated according to (2.3), and the threshold used for the subsequent triggering decision is then computed as

$$\varepsilon_{k+1} = \frac{\varepsilon_0}{1 + \eta r_{k+1}}, \tag{2.4}$$

where $\varepsilon_0 > 0$ is the nominal triggering threshold, and $\eta \geq 0$ is the loss-adjustment coefficient. Thus, ε_{k+1} is the loss-adapted triggering threshold and remains unchanged until the next event is generated. It follows from (2.4) that

$$0 < \varepsilon_{k+1} \leq \varepsilon_0. \tag{2.5}$$

When $\eta = 0$, the mechanism reduces to a fixed-threshold design. For $\eta > 0$, a longer sequence of consecutive packet losses results in a smaller ε_{k+1}, thereby lowering the threshold for the next transmission attempt.

Remark 1. *In the considered architecture, $\sigma(t_k)$ denotes the delivery status explicitly confirmed by the communication interface for the packet transmitted at t_k. The communication interface completes the status-resolution procedure and provides $\sigma(t_k)$ to the field-side triggering unit before the next admissible triggering test at $t_k + T_{\min}$. Upon receiving this status, the triggering unit sequentially updates r_{k+1} and ε_{k+1} before determining t_{k+1}. An acknowledgment delay or loss may postpone or prevent these updates and thereby alter the subsequent triggering sequence. Explicit treatment of delayed or unreliable acknowledgment feedback would require extending the current network model and the corresponding stability analysis.*

The encoder and Decoder 2 are co-located at the field-side node. Therefore, the scale $s(t_k)$ is retained and shared locally, whereas only the finite-bit index vector is transmitted through the

sensor-to-controller channel. In the communication metrics, N_{tx} counts sensor-to-controller transmission attempts, and $n_y b_z$ denotes the payload length of each triggered packet. These metrics cover the sensor-to-controller data link; reception-status signaling and controller-to-actuator communication lie outside their scope.

Using (2.2) and (2.4), the next triggering instant is determined by

$$t_{k+1} = \inf\left\{t \geq t_k + T_{\min} \,\middle|\, e_y^{\mathrm{T}}(t)\mathbf{W}e_y(t) \geq \varepsilon_{k+1} y^{\mathrm{T}}(t)\mathbf{W}y(t)\right\}, \tag{2.6}$$

where $\mathbf{W} = \mathbf{W}^{\mathrm{T}} > 0$ is the triggering weight matrix. Let

$$\mathcal{T}_k^{(1)} = [t_k, t_k + T_{\min}),\ \mathcal{T}_k^{(2)} = [t_k + T_{\min}, t_{k+1}).$$

For $t \in \mathcal{T}_k^{(1)}$, set $\Delta(t) = t - t_k$, and define

$$\psi(t) = \begin{cases} \dfrac{1}{\Delta(t)} \displaystyle\int_{t_k}^{t} \dot{x}(\lambda)\, d\lambda, & \Delta(t) > 0, \\ \dot{x}(t_k^+), & \Delta(t) = 0, \end{cases}$$

where t_k^+ denotes the right-hand limit at t_k. Therefore, the sampled state $x(t_k)$ can be represented as

$$x(t_k) = x(t) - \Delta(t)\psi(t). \tag{2.7}$$

The output sampling error $e_y(t)$ is defined as

$$e_y(t) = \begin{cases} -\mathbf{C}\Delta(t)\psi(t), & t \in \mathcal{T}_k^{(1)}, \\ \mathbf{C}(x(t_k) - x(t)), & t \in \mathcal{T}_k^{(2)}. \end{cases} \tag{2.8}$$

For $t \in \mathcal{T}_k^{(2)}$, the triggering condition remains unsatisfied. Hence, (2.5) and (2.6) yield

$$e_y^{\mathrm{T}}(t)\mathbf{W}e_y(t) \leq \varepsilon_0 x^{\mathrm{T}}(t)\mathbf{C}^{\mathrm{T}}\mathbf{W}\mathbf{C}x(t). \tag{2.9}$$

Algorithm 1 summarizes the causal implementation sequence of PLAETM. The packet-reception status associated with the transmission at t_k becomes available before the next admissible triggering test. The triggering unit then updates r_{k+1} and ε_{k+1} sequentially before determining t_{k+1}.

Algorithm 1. Update procedure of PLAETM

Input: Measured output $y(t)$, packet-reception status $\sigma(t_k)$, and parameters $T_{\min}$, ε_0, η, and $\mathbf{W}$.
Output: Triggering instants $\{t_k\}_{k\geq 0}$, consecutive-loss counters $\{r_k\}_{k\geq 0}$, and triggering thresholds $\{\varepsilon_k\}_{k\geq 0}$.

1: Initialize $t_0 = 0$ and $r_0 = 0$.
2: **for** $k = 0, 1, 2, \ldots$ **do**
3: Release $y(t_k)$ for encoding and transmission.
4: Obtain $\sigma(t_k)$ before $t_k + T_{\min}$.
5: Update r_{k+1} according to (2.3).
6: Update ε_{k+1} according to (2.4).
7: Determine t_{k+1} according to (2.6).
8: **end for**

2.3. SNEDM

At each triggering instant, SNEDM maps the sampled output into a bounded normalized domain and represents the normalized vector by a finite-bit index vector. The encoding and reconstruction procedures are formulated as follows.

When an event is triggered at t_k, the sampled output is written as

$$y(t_k) = \begin{bmatrix} y_1(t_k) & y_2(t_k) & \cdots & y_{n_y}(t_k) \end{bmatrix}^{\mathrm{T}}.$$

The scale factor is selected as

$$s(t_k) = \max\{s_{\min}, \|y(t_k)\|_\infty\}, \tag{2.10}$$

where $s_{\min} > 0$ is the prescribed lower bound for the scale. In the considered architecture, the encoder and Decoder 2 are co-located at the field-side node. Thus, the scale $s(t_k)$ in (2.10) is retained locally and used by Decoder 2 for scale recovery, whereas only the finite-bit normalized index vector is transmitted through the bandwidth-limited sensor-to-controller channel.

Using the scale factor in (2.10), the ith output component is normalized as

$$z_i(t_k) = \frac{y_i(t_k)}{s(t_k)}, \qquad i = 1, 2, \ldots, n_y. \tag{2.11}$$

The normalized output vector is represented by

$$z(t_k) = \begin{bmatrix} z_1(t_k) & z_2(t_k) & \cdots & z_{n_y}(t_k) \end{bmatrix}^{\mathrm{T}}.$$

It follows from (2.10) and (2.11) that

$$|z_i(t_k)| \le 1, \qquad i = 1, 2, \ldots, n_y,$$

which further implies

$$\|z(t_k)\|_\infty \le 1.$$

Let $b_z \ge 2$ denote the number of bits assigned to each normalized component, and define

$$q_z = 2^{b_z}.$$

Because $\|z(t_k)\|_\infty \le 1$, the normalized domain $[-1, 1]$ is uniformly divided into q_z subintervals, and the jth subinterval $\mathcal{Q}_j$ is expressed as

$$\mathcal{Q}_j = \left[-1 + \frac{2j}{q_z}, -1 + \frac{2(j+1)}{q_z}\right), \qquad j = 0, 1, \ldots, q_z - 1, \tag{2.12}$$

where the last subinterval is closed at the right endpoint such that $1 \in \mathcal{Q}_{q_z-1}$.

According to (2.10) and (2.12), the width of each quantization interval in the physical output domain is $2s(t_k)/q_z$. When $\|y(t_k)\|_\infty < s_{\min}$, the scale satisfies $s(t_k) = s_{\min}$, so a smaller $s_{\min}$ provides finer reconstruction resolution near the origin, whereas a larger $s_{\min}$ enlarges the minimum physical quantization range with a coarser resolution. When $\|y(t_k)\|_\infty \ge s_{\min}$, the scale follows the current output magnitude, and the instantaneous quantization range is determined by $\|y(t_k)\|_\infty$.

For each normalized component, the zero-based transmitted index $m_i(t_k) \in \{0, 1, \ldots, q_z - 1\}$ is determined according to (2.12) as

$$z_i(t_k) \in \mathcal{Q}_{m_i(t_k)}, \qquad i = 1, 2, \ldots, n_y. \tag{2.13}$$

Because each $m_i(t_k)$ is represented by b_z bits, the encoded index vector is written as

$$m(t_k) = \begin{bmatrix} m_1(t_k) & m_2(t_k) & \cdots & m_{n_y}(t_k) \end{bmatrix}^{\mathrm{T}}.$$

Only $m(t_k)$ is transmitted through the sensor-to-controller channel, and the corresponding payload length is $n_y b_z$ bits for each triggered packet. According to (2.12) and (2.13), the midpoint reconstruction associated with $m_i(t_k)$ is expressed as

$$\widehat{z}_i(t_k) = -1 + \frac{2m_i(t_k) + 1}{q_z}, \qquad i = 1, 2, \ldots, n_y. \tag{2.14}$$

The corresponding reconstructed normalized vector is represented by

$$\widehat{z}(t_k) = \begin{bmatrix} \widehat{z}_1(t_k) & \widehat{z}_2(t_k) & \cdots & \widehat{z}_{n_y}(t_k) \end{bmatrix}^{\mathrm{T}}.$$

Using the scale factor in (2.10) and the reconstructed normalized vector in (2.14), the reconstructed physical output is expressed as

$$\widehat{y}(t_k) = s(t_k)\widehat{z}(t_k). \tag{2.15}$$

Based on the reconstructed normalized output, the edge controller computes

$$u_z(t_k) = -\mathbf{K}\widehat{z}(t_k), \tag{2.16}$$

where $\mathbf{K} \in \mathbb{R}^{n_u \times n_y}$ is the output-feedback gain. Using the scale factor in (2.10), Decoder 2 reconstructs the physical control command as

$$\bar{u}(t_k) = s(t_k)u_z(t_k). \tag{2.17}$$

The output reconstruction error is defined as

$$e_q(t_k) = \widehat{y}(t_k) - y(t_k).$$

Using (2.15)–(2.17) and the definition of $e_q(t_k)$, the actual control input is expressed as

$$u(t) = \sigma(t_k)\bar{u}(t_k) = -\sigma(t_k)\mathbf{K}(y(t_k) + e_q(t_k)). \tag{2.18}$$

Using (2.1) and (2.18), the closed-loop dynamics on $\mathcal{T}_k^{(1)}$ are expressed as

$$\dot{x}(t) = \mathbf{A}x(t) - \sigma(t_k)\mathbf{BKC}x(t_k) - \sigma(t_k)\mathbf{BK}e_q(t_k). \tag{2.19}$$

Substituting (2.7) into (2.19) yields

$$\dot{x}(t) = (\mathbf{A} - \sigma(t_k)\mathbf{BKC})x(t) + \sigma(t_k)\mathbf{BKC}\Delta(t)\psi(t) - \sigma(t_k)\mathbf{BK}e_q(t_k), \qquad t \in \mathcal{T}_k^{(1)}. \tag{2.20}$$

For $t \in \mathcal{T}_k^{(2)}$, the second branch of (2.8) gives

$$y(t_k) = y(t) + e_y(t). \tag{2.21}$$

Using (2.21) and the output equation in (2.1), the sampled output is rewritten as

$$y(t_k) = \mathbf{C}x(t) + e_y(t).$$

Substituting this expression into (2.18) and then using (2.1) yields

$$\dot{x}(t) = (\mathbf{A} - \sigma(t_k)\mathbf{BKC})x(t) - \sigma(t_k)\mathbf{BK}e_y(t) - \sigma(t_k)\mathbf{BK}e_q(t_k), \qquad t \in \mathcal{T}_k^{(2)}. \tag{2.22}$$

Remark 2. *The actuator adopts a zero-order hold between consecutive triggering instants. Under* (2.18)*, a successfully received command is held over the corresponding interevent interval, whereas a packet loss results in zero input. A hold-last-command strategy can preserve control continuity after packet loss, but the retained command may become increasingly outdated as the plant state evolves. Therefore, the zero-input policy is adopted here to avoid prolonged actuation based on stale output information.*

Definition 1. *The stochastic closed-loop system under Bernoulli packet losses described by* (2.20) *and* (2.22) *is said to satisfy MSEUB if there exist constants $c_1 > 0$, $c_2 > 0$, and $c_3 > 0$ such that*

$$\mathbb{E}\{\|x(t)\|^2\} \le c_1 e^{-c_2(t-t_0)}\mathbb{E}\{\|x(t_0)\|^2\} + c_3$$

for all $t \ge t_0$.

Lemma 1. *Suppose that the scale factor $s(t_k)$ is generated by* (2.10) *and that the normalized output is encoded and reconstructed according to* (2.12)–(2.14)*. Then, there exists a constant $\kappa_q = n_y/q_z^2 > 0$, independent of t_k, such that*

$$e_q^{\mathrm{T}}(t_k)e_q(t_k) \le \kappa_q \left[s_{\min}^2 + y^{\mathrm{T}}(t_k)y(t_k)\right]. \tag{2.23}$$

Proof. Each normalized component is reconstructed by the midpoint of an interval with width $2/q_z$. Hence, $|\widehat{z}_i(t_k) - z_i(t_k)| \le 1/q_z$ for $i = 1, 2, \ldots, n_y$, and

$$\|\widehat{z}(t_k) - z(t_k)\|^2 \le \frac{n_y}{q_z^2} = \kappa_q.$$

Because $e_q(t_k) = s(t_k)[\widehat{z}(t_k) - z(t_k)]$,

$$e_q^{\mathrm{T}}(t_k)e_q(t_k) \le \kappa_q s^2(t_k).$$

Moreover, (2.10) gives

$$s^2(t_k) = \max\left\{s_{\min}^2, \|y(t_k)\|_\infty^2\right\} \le s_{\min}^2 + y^{\mathrm{T}}(t_k)y(t_k).$$

Combining these inequalities establishes (2.23). □

Lemma 2. *[41] For a positive integer N, let $\mathbf{\Lambda}$, $\mathbf{U}_i$, and $\mathbf{V}_i$ be dimensionally compatible real matrices, and let $\mathbf{R}_i$ be nonsingular, $i = 1, \ldots, N$. The inequality*

$$\mathbf{\Lambda} + \sum_{i=1}^{N} \mathrm{He}\left(\mathbf{U}_i\mathbf{R}_i^{-1}\mathbf{V}_i^{\mathrm{T}}\right) < 0 \tag{2.24}$$

holds if there are scalars $\rho_i > 0$, $i = 1, \ldots, N$ such that

$$\begin{bmatrix} \mathbf{\Lambda} & \mathbf{U}_1 + \rho_1\mathbf{V}_1 & \cdots & \mathbf{U}_N + \rho_N\mathbf{V}_N \\ * & \mathrm{diag}\{-\rho_1\,\mathrm{He}(\mathbf{R}_1), \ldots, -\rho_N\,\mathrm{He}(\mathbf{R}_N)\} & & \end{bmatrix} < 0. \tag{2.25}$$

3. Main results

Let $\mathcal{F}_k^-$ denote the history information set before the packet-reception status $\sigma(t_k)$ is observed. The packet-reception process is assumed to satisfy

$$\mathbb{P}\{\sigma(t_k) = 1 \mid \mathcal{F}_k^-\} = p_s. \tag{3.1}$$

To separate the mean reception probability from its random fluctuation, define

$$\xi_k = \sigma(t_k) - p_s, \qquad \mathbb{E}\{\xi_k \mid \mathcal{F}_k^-\} = 0, \qquad \mathbb{E}\{\xi_k^2 \mid \mathcal{F}_k^-\} = \nu_s, \tag{3.2}$$

where

$$\nu_s = p_s(1 - p_s).$$

Remark 3. *The conditional reception model in* (3.1) *describes a memoryless packet-reception process with a constant success probability p_s. The conditional moments in* (3.2) *are therefore independent of previous reception outcomes. Temporally correlated or bursty packet losses, including Markovian and Gilbert–Elliott channels, require a channel-mode-dependent model. In this case, the stability analysis needs to account for different channel modes and their transitions. The PLAETM loss counter remains updateable from the observed reception sequence.*

Theorem 1. *Assume that the packet-reception process satisfies* (3.1) *and that the encoding–decoding scheme satisfies the conditions of Lemma 1. For given $b_z \geq 2$; $s_{\min} > 0$, $\mathbf{K} \in \mathbb{R}^{n_u \times n_y}$; and $\varepsilon_0, T_{\min}, \alpha, \tau_1, \tau_2 > 0$, define $q_z = 2^{b_z}$ and $\kappa_q = n_y/q_z^2$. If there exist $\mathbf{P} = \mathbf{P}^{\mathrm{T}} > 0$ and $\mathbf{S} = \mathbf{S}^{\mathrm{T}} > 0$ in $\mathbb{R}^{n_x \times n_x}$; $\mathbf{W} = \mathbf{W}^{\mathrm{T}} > 0$ in $\mathbb{R}^{n_y \times n_y}$, $\mathbf{Z}, \mathbf{Z}_1, \mathbf{N}_3 \in \mathbb{R}^{n_x \times n_x}$, $\mathbf{M}_i, \mathbf{F}_i, \mathbf{N}_i \in \mathbb{R}^{n_x \times n_x}$ for $i \in \{1, 2\}$; and $\mu_q > 0$ such that the following matrix inequalities hold:*

$$\begin{bmatrix} \mathbf{P} + T_{\min}\dfrac{\mathrm{He}(\mathbf{Z})}{2} & T_{\min}(\mathbf{Z}_1 - \mathbf{Z}) \\ * & -T_{\min}\,\mathrm{He}(\mathbf{Z}_1) + T_{\min}\dfrac{\mathrm{He}(\mathbf{Z})}{2} \end{bmatrix} \succ 0, \tag{3.3a}$$

$$\boldsymbol{\Phi}_0^{\sigma} = \begin{bmatrix} \boldsymbol{\Phi}_{11}(0) & \boldsymbol{\Phi}_{12}(0) & \boldsymbol{\Phi}_{13}(0) & -p_s\mathbf{M}_1^{\mathrm{T}}\mathbf{B}\mathbf{K} & \tau_1\mathbf{M}_1^{\mathrm{T}} & 0 \\ * & \boldsymbol{\Phi}_{22}(0) & \boldsymbol{\Phi}_{23}(0) & -p_s\mathbf{M}_2^{\mathrm{T}}\mathbf{B}\mathbf{K} & \tau_1\mathbf{M}_2^{\mathrm{T}} & 0 \\ * & * & \boldsymbol{\Phi}_{33}^{q}(0) & 0 & 0 & \sqrt{\nu_s}(\mathbf{B}\mathbf{K}\mathbf{C})^{\mathrm{T}} \\ * & * & * & -\mu_q\mathbf{I}_{n_y} & 0 & \sqrt{\nu_s}(\mathbf{B}\mathbf{K})^{\mathrm{T}} \\ * & * & * & * & -\tau_1\mathbf{I}_{n_x} & 0 \\ * & * & * & * & * & -\tau_1\mathbf{I}_{n_x} \end{bmatrix} \prec 0, \tag{3.3b}$$

$$\boldsymbol{\Phi}_{T_{\min}}^{\sigma} = \begin{bmatrix} \boldsymbol{\Phi}_{11}(T_{\min}) & \boldsymbol{\Phi}_{12}(T_{\min}) & \boldsymbol{\Phi}_{13}(T_{\min}) & T_{\min}\mathbf{N}_1 & -p_s\mathbf{M}_1^{\mathrm{T}}\mathbf{B}\mathbf{K} & \tau_1\mathbf{M}_1^{\mathrm{T}} & 0 \\ * & \boldsymbol{\Phi}_{22}(T_{\min}) & \boldsymbol{\Phi}_{23}(T_{\min}) & T_{\min}\mathbf{N}_2 & -p_s\mathbf{M}_2^{\mathrm{T}}\mathbf{B}\mathbf{K} & \tau_1\mathbf{M}_2^{\mathrm{T}} & 0 \\ * & * & \boldsymbol{\Phi}_{33}^{q}(T_{\min}) & T_{\min}\mathbf{N}_3 & 0 & 0 & \sqrt{\nu_s}(\mathbf{B}\mathbf{K}\mathbf{C})^{\mathrm{T}} \\ * & * & * & -T_{\min}e^{-2\alpha T_{\min}}\mathbf{S} & 0 & 0 & 0 \\ * & * & * & * & -\mu_q\mathbf{I}_{n_y} & 0 & \sqrt{\nu_s}(\mathbf{B}\mathbf{K})^{\mathrm{T}} \\ * & * & * & * & * & -\tau_1\mathbf{I}_{n_x} & 0 \\ * & * & * & * & * & * & -\tau_1\mathbf{I}_{n_x} \end{bmatrix} \prec 0, \tag{3.3c}$$

$$\boldsymbol{\Theta}^{\sigma} = \begin{bmatrix} \boldsymbol{\Theta}_{11}^{q} & \boldsymbol{\Theta}_{12} & \boldsymbol{\Theta}_{13}^{q} & -p_s\mathbf{F}_1^{\mathrm{T}}\mathbf{BK} & \tau_2\mathbf{F}_1^{\mathrm{T}} & \sqrt{\nu_s}(\mathbf{BKC})^{\mathrm{T}} \\ * & -\mathrm{He}(\mathbf{F}_2) & -p_s\mathbf{F}_2^{\mathrm{T}}\mathbf{BK} & -p_s\mathbf{F}_2^{\mathrm{T}}\mathbf{BK} & \tau_2\mathbf{F}_2^{\mathrm{T}} & 0 \\ * & * & \boldsymbol{\Theta}_{33}^{q} & 0 & 0 & \sqrt{\nu_s}(\mathbf{BK})^{\mathrm{T}} \\ * & * & * & -\mu_q\mathbf{I}_{n_y} & 0 & \sqrt{\nu_s}(\mathbf{BK})^{\mathrm{T}} \\ * & * & * & * & -\tau_2\mathbf{I}_{n_x} & 0 \\ * & * & * & * & * & -\tau_2\mathbf{I}_{n_x} \end{bmatrix} < 0, \tag{3.3d}$$

where

$$\begin{aligned}
\boldsymbol{\Phi}_{11}(\Delta(t)) &= \mathrm{He}(\mathbf{M}_1^{\mathrm{T}}\mathbf{A}) + 2\alpha\mathbf{P} - \mathrm{He}(\mathbf{N}_1) - [1 - 2\alpha(T_{\min} - \Delta(t))]\frac{\mathrm{He}(\mathbf{Z})}{2}, \\
\boldsymbol{\Phi}_{12}(\Delta(t)) &= \mathbf{P} - \mathbf{M}_1^{\mathrm{T}} + \mathbf{A}^{\mathrm{T}}\mathbf{M}_2 - \mathbf{N}_2^{\mathrm{T}} + (T_{\min} - \Delta(t))\frac{\mathrm{He}(\mathbf{Z})}{2}, \\
\boldsymbol{\Phi}_{13}(\Delta(t)) &= \mathbf{N}_1 - p_s\mathbf{M}_1^{\mathrm{T}}\mathbf{BKC} - \mathbf{N}_3^{\mathrm{T}} + [1 - 2\alpha(T_{\min} - \Delta(t))](\mathbf{Z} - \mathbf{Z}_1), \\
\boldsymbol{\Phi}_{22}(\Delta(t)) &= -\mathrm{He}(\mathbf{M}_2) + (T_{\min} - \Delta(t))\mathbf{S}, \\
\boldsymbol{\Phi}_{23}(\Delta(t)) &= \mathbf{N}_2 - p_s\mathbf{M}_2^{\mathrm{T}}\mathbf{BKC} - (T_{\min} - \Delta(t))(\mathbf{Z} - \mathbf{Z}_1), \\
\boldsymbol{\Phi}_{33}(\Delta(t)) &= \mathrm{He}(\mathbf{N}_3) + [1 - 2\alpha(T_{\min} - \Delta(t))]\left[\mathrm{He}(\mathbf{Z}_1) - \frac{\mathrm{He}(\mathbf{Z})}{2}\right], \\
\boldsymbol{\Phi}_{33}^{q}(\Delta(t)) &= \boldsymbol{\Phi}_{33}(\Delta(t)) + \mu_q\kappa_q\mathbf{C}^{\mathrm{T}}\mathbf{C}, \\
\boldsymbol{\Theta}_{11}^{q} &= 2\alpha\mathbf{P} + \varepsilon_0\mathbf{C}^{\mathrm{T}}\mathbf{WC} + \mu_q\kappa_q\mathbf{C}^{\mathrm{T}}\mathbf{C} + \mathrm{He}\left[\mathbf{F}_1^{\mathrm{T}}(\mathbf{A} - p_s\mathbf{BKC})\right], \\
\boldsymbol{\Theta}_{13}^{q} &= -p_s\mathbf{F}_1^{\mathrm{T}}\mathbf{BK} + \mu_q\kappa_q\mathbf{C}^{\mathrm{T}}, \\
\boldsymbol{\Theta}_{33}^{q} &= -\mathbf{W} + \mu_q\kappa_q\mathbf{I}_{n_y}, \\
\boldsymbol{\Theta}_{12} &= \mathbf{P} - \mathbf{F}_1^{\mathrm{T}} + (\mathbf{A} - p_s\mathbf{BKC})^{\mathrm{T}}\mathbf{F}_2,
\end{aligned}$$

then the closed-loop system in (2.20) *and* (2.22) *under Bernoulli packet losses satisfies MSEUB and*

$$\limsup_{t\to\infty} \mathbb{E}\{\|x(t)\|^2\} \le \frac{\mu_q\kappa_q s_{\min}^2}{2\alpha\underline{c}},$$

where

$$\underline{c} = \min\left\{\lambda_{\min}(\mathbf{P}), \lambda_{\min}\left(\begin{bmatrix} \mathbf{P} + T_{\min}\dfrac{\mathrm{He}(\mathbf{Z})}{2} & T_{\min}(\mathbf{Z}_1 - \mathbf{Z}) \\ * & -T_{\min}\,\mathrm{He}(\mathbf{Z}_1) + T_{\min}\dfrac{\mathrm{He}(\mathbf{Z})}{2} \end{bmatrix}\right)\right\}.$$

It follows from (3.3a) *that* $\underline{c} > 0$.

Proof. Case 1: $t \in \mathcal{T}_k^{(1)}$.

To analyze the first subinterval in (2.20), introduce the Lyapunov–Krasovskii functional

$$\mathcal{V}_1(t) = \mathcal{V}_1^P(t) + \mathcal{V}_1^S(t) + \mathcal{V}_1^H(t),$$

where

$$\mathcal{V}_1^P(t) = x^{\mathrm{T}}(t)\mathbf{P}x(t),$$

$$\mathcal{V}_1^S(t) = (T_{\min} - \Delta(t)) \int_{t_k}^{t} e^{2\alpha(\lambda - t)} \dot{x}^{\mathrm{T}}(\lambda) \mathbf{S} \dot{x}(\lambda)\, d\lambda,$$
$$\mathcal{V}_1^H(t) = (T_{\min} - \Delta(t)) \begin{bmatrix} x^{\mathrm{T}}(t) & x^{\mathrm{T}}(t_k) \end{bmatrix} \mathbf{H}_0 \begin{bmatrix} x^{\mathrm{T}}(t) & x^{\mathrm{T}}(t_k) \end{bmatrix}^{\mathrm{T}},$$

and

$$\mathbf{H}_0 = \begin{bmatrix} \dfrac{\mathrm{He}(\mathbf{Z})}{2} & \mathbf{Z}_1 - \mathbf{Z} \\ * & -\mathrm{He}(\mathbf{Z}_1) + \dfrac{\mathrm{He}(\mathbf{Z})}{2} \end{bmatrix}.$$

Condition (3.3a) can be expressed as

$$\begin{bmatrix} \mathbf{P} & 0 \\ 0 & 0 \end{bmatrix} + T_{\min} \mathbf{H}_0 \succ 0.$$

For $0 \le \Delta(t) \le T_{\min}$, the matrix associated with $\mathcal{V}_1^P(t) + \mathcal{V}_1^H(t)$ satisfies

$$\begin{bmatrix} \mathbf{P} & 0 \\ 0 & 0 \end{bmatrix} + (T_{\min} - \Delta(t)) \mathbf{H}_0 = \frac{\Delta(t)}{T_{\min}} \begin{bmatrix} \mathbf{P} & 0 \\ 0 & 0 \end{bmatrix} + \frac{T_{\min} - \Delta(t)}{T_{\min}} \left(\begin{bmatrix} \mathbf{P} & 0 \\ 0 & 0 \end{bmatrix} + T_{\min} \mathbf{H}_0 \right).$$

This representation is a convex combination of two positive semidefinite matrices, with the second matrix being positive definite. Thus, $\mathcal{V}_1^P(t) + \mathcal{V}_1^H(t)$ is positive definite with respect to $x(t)$. At $\Delta(t) = T_{\min}$, the same sum reduces to $x^{\mathrm{T}}(t)\mathbf{P}x(t)$. The conditions $\mathbf{S} \succ 0$ and $T_{\min} - \Delta(t) \ge 0$ also ensure $\mathcal{V}_1^S(t) \ge 0$. These properties establish the positive definiteness of $\mathcal{V}_1(t)$ with respect to $x(t)$.

At $t = t_k$, the integral term in $\mathcal{V}_1^S(t)$ vanishes. In addition,

$$\begin{bmatrix} \mathbf{I} & \mathbf{I} \end{bmatrix} \mathbf{H}_0 \begin{bmatrix} \mathbf{I} & \mathbf{I} \end{bmatrix}^{\mathrm{T}} = 0.$$

The initial value of the functional is therefore

$$\mathcal{V}_1(t_k) = x^{\mathrm{T}}(t_k)\mathbf{P}x(t_k).$$

Differentiating the three functional components gives

$$\dot{\mathcal{V}}_1^P(t) = 2x^{\mathrm{T}}(t)\mathbf{P}\dot{x}(t),$$

$$\dot{\mathcal{V}}_1^S(t) = -\int_{t_k}^{t} e^{2\alpha(\lambda - t)} \dot{x}^{\mathrm{T}}(\lambda) \mathbf{S} \dot{x}(\lambda)\, d\lambda + (T_{\min} - \Delta(t)) \dot{x}^{\mathrm{T}}(t) \mathbf{S} \dot{x}(t) - 2\alpha \mathcal{V}_1^S(t), \tag{3.4}$$

and

$$\dot{\mathcal{V}}_1^H(t) = -\begin{bmatrix} x^{\mathrm{T}}(t) & x^{\mathrm{T}}(t_k) \end{bmatrix} \mathbf{H}_0 \begin{bmatrix} x^{\mathrm{T}}(t) & x^{\mathrm{T}}(t_k) \end{bmatrix}^{\mathrm{T}} + 2(T_{\min} - \Delta(t)) \begin{bmatrix} \dot{x}^{\mathrm{T}}(t) & 0 \end{bmatrix} \mathbf{H}_0 \begin{bmatrix} x^{\mathrm{T}}(t) & x^{\mathrm{T}}(t_k) \end{bmatrix}^{\mathrm{T}}.$$

For $\lambda \in [t_k, t]$, the exponential weighting term satisfies

$$e^{2\alpha(\lambda - t)} \ge e^{-2\alpha T_{\min}}.$$

Applying Jensen's inequality to the weighted integral in (3.4) yields

$$-\int_{t_k}^{t} e^{2\alpha(\lambda - t)} \dot{x}^{\mathrm{T}}(\lambda) \mathbf{S} \dot{x}(\lambda)\, d\lambda \le -\Delta(t) e^{-2\alpha T_{\min}} \psi^{\mathrm{T}}(t) \mathbf{S} \psi(t).$$

To isolate the packet-dependent control input, define

$$d_k = \mathbf{BK}\left[\mathbf{C}x(t_k) + e_q(t_k)\right]. \tag{3.5}$$

To introduce the free matrices $\mathbf{M}_1$ and $\mathbf{M}_2$, substitute $\sigma(t_k) = p_s + \xi_k$ into the first closed-loop equation, and add the following zero identity:

$$0 = 2[x^{\mathrm{T}}(t)\mathbf{M}_1^{\mathrm{T}} + \dot{x}^{\mathrm{T}}(t)\mathbf{M}_2^{\mathrm{T}}][\mathbf{A}x(t) - p_s d_k - \dot{x}(t)] - 2\xi_k[x^{\mathrm{T}}(t)\mathbf{M}_1^{\mathrm{T}} + \dot{x}^{\mathrm{T}}(t)\mathbf{M}_2^{\mathrm{T}}]d_k. \tag{3.6}$$

To introduce the free matrices $\mathbf{N}_1$, $\mathbf{N}_2$, and $\mathbf{N}_3$, use the state integral identity

$$0 = 2[x^{\mathrm{T}}(t)\mathbf{N}_1 + \dot{x}^{\mathrm{T}}(t)\mathbf{N}_2 + x^{\mathrm{T}}(t_k)\mathbf{N}_3] \times [x(t_k) - x(t) + \Delta(t)\psi(t)].$$

The random cross term in (3.6) is bounded through Young's inequality. For $\tau_1 > 0$,

$$-2\xi_k[x^{\mathrm{T}}(t)\mathbf{M}_1^{\mathrm{T}} + \dot{x}^{\mathrm{T}}(t)\mathbf{M}_2^{\mathrm{T}}]d_k \le \tau_1\|\mathbf{M}_1 x(t) + \mathbf{M}_2\dot{x}(t)\|^2 + \frac{\xi_k^2}{\tau_1}d_k^{\mathrm{T}}d_k. \tag{3.7}$$

The vector d_k depends only on information available before the current packet-reception status. It is therefore $\mathcal{F}_k^-$-measurable. Taking the conditional expectation of (3.7) and applying (3.2) gives

$$\mathbb{E}\left\{-2\xi_k[\mathbf{M}_1 x(t) + \mathbf{M}_2\dot{x}(t)]^{\mathrm{T}}d_k \mid \mathcal{F}_k^-\right\} \le \tau_1\mathbb{E}\left\{\|\mathbf{M}_1 x(t) + \mathbf{M}_2\dot{x}(t)\|^2 \mid \mathcal{F}_k^-\right\} + \frac{\nu_s}{\tau_1}d_k^{\mathrm{T}}d_k.$$

Arrange the derivative terms according to

$$\left[x^{\mathrm{T}}(t) \quad \dot{x}^{\mathrm{T}}(t) \quad x^{\mathrm{T}}(t_k) \quad \psi^{\mathrm{T}}(t) \quad e_q^{\mathrm{T}}(t_k)\right]^{\mathrm{T}}.$$

The resulting symmetric coefficient matrix depends affinely on $\Delta(t)$.

At $\Delta(t) = 0$, the blocks associated with $\psi(t)$ vanish. The reduced coefficient matrix over the active variables is negative definite according to (3.3b). Restoring the zero row and column associated with $\psi(t)$ yields a negative-semidefinite extension. At $\Delta(t) = T_{\min}$, the coefficient matrix is negative definite according to (3.3c). Because the coefficient matrix is affine in $\Delta(t)$, it is a convex combination of these endpoint matrices for $0 \le \Delta(t) \le T_{\min}$. It is therefore negative semidefinite and is negative definite over the active-variable subspace. The Schur complements of (3.3b) and (3.3c) establish

$$\mathbb{E}\{\dot{\mathcal{V}}_1(t) + 2\alpha\mathcal{V}_1(t) - \mu_q e_q^{\mathrm{T}}(t_k)e_q(t_k) + \mu_q\kappa_q x^{\mathrm{T}}(t_k)\mathbf{C}^{\mathrm{T}}\mathbf{C}x(t_k)\} \le 0.$$

Using (2.23) with $y(t_k) = \mathbf{C}x(t_k)$ gives

$$\mathbb{E}\left\{\dot{\mathcal{V}}_1(t) + 2\alpha\mathcal{V}_1(t)\right\} \le \mu_q\kappa_q s_{\min}^2. \tag{3.8}$$

Case 2: $t \in \mathcal{T}_k^{(2)}$.

To analyze the second subinterval, consider the quadratic Lyapunov function

$$\mathcal{V}_2(t) = x^{\mathrm{T}}(t)\mathbf{P}x(t).$$

Its derivative satisfies

$$\dot{\mathcal{V}}_2(t) = 2x^{\mathrm{T}}(t)\mathbf{P}\dot{x}(t). \tag{3.9}$$

The relation $\mathbf{C}x(t) + e_y(t) = \mathbf{C}x(t_k)$ holds on $\mathcal{T}_k^{(2)}$. Accordingly, the packet-dependent control term in (3.5) can be expressed as

$$d_k = \mathbf{BK}\left[\mathbf{C}x(t) + e_y(t) + e_q(t_k)\right].$$

To introduce the free matrices $\mathbf{F}_1$ and $\mathbf{F}_2$, substitute $\sigma(t_k) = p_s + \xi_k$ into the second closed-loop equation, and add the following zero identity:

$$\begin{aligned} 0 = {} & 2[x^{\mathrm{T}}(t)\mathbf{F}_1^{\mathrm{T}} + \dot{x}^{\mathrm{T}}(t)\mathbf{F}_2^{\mathrm{T}}] \times [(\mathbf{A} - p_s\mathbf{BKC})x(t) - p_s\mathbf{BK}e_y(t) - p_s\mathbf{BK}e_q(t_k) - \dot{x}(t)] \\ & - 2\xi_k[x^{\mathrm{T}}(t)\mathbf{F}_1^{\mathrm{T}} + \dot{x}^{\mathrm{T}}(t)\mathbf{F}_2^{\mathrm{T}}]d_k. \end{aligned} \tag{3.10}$$

The random cross term in (3.10) is bounded through Young's inequality. For $\tau_2 > 0$,

$$-2\xi_k[x^{\mathrm{T}}(t)\mathbf{F}_1^{\mathrm{T}} + \dot{x}^{\mathrm{T}}(t)\mathbf{F}_2^{\mathrm{T}}]d_k \le \tau_2\|\mathbf{F}_1x(t) + \mathbf{F}_2\dot{x}(t)\|^2 + \frac{\xi_k^2}{\tau_2}d_k^{\mathrm{T}}d_k.$$

The vector d_k remains $\mathcal{F}_k^-$-measurable. Taking the conditional expectation and applying (3.2) gives

$$\mathbb{E}\left\{-2\xi_k[\mathbf{F}_1x(t) + \mathbf{F}_2\dot{x}(t)]^{\mathrm{T}}d_k \mid \mathcal{F}_k^-\right\} \le \tau_2\mathbb{E}\left\{\|\mathbf{F}_1x(t) + \mathbf{F}_2\dot{x}(t)\|^2 \mid \mathcal{F}_k^-\right\} + \frac{\nu_s}{\tau_2}d_k^{\mathrm{T}}d_k.$$

Combine this inequality with (2.9) and (3.9). Arrange the resulting terms according to

$$\begin{bmatrix} x^{\mathrm{T}}(t) & \dot{x}^{\mathrm{T}}(t) & e_y^{\mathrm{T}}(t) & e_q^{\mathrm{T}}(t_k) \end{bmatrix}^{\mathrm{T}}.$$

The associated coefficient matrix is the Schur complement of $\mathbf{\Theta}^\sigma$ in (3.3d). The Schur complement of $\mathbf{\Theta}^\sigma$ establishes

$$\mathbb{E}\{\dot{\mathcal{V}}_2(t) + 2\alpha\mathcal{V}_2(t) - \mu_q e_q^{\mathrm{T}}(t_k)e_q(t_k) + \mu_q\kappa_q[\mathbf{C}x(t) + e_y(t)]^{\mathrm{T}}[\mathbf{C}x(t) + e_y(t)]\} \le 0.$$

Using (2.23) with $y(t_k) = \mathbf{C}x(t) + e_y(t)$ gives

$$\mathbb{E}\left\{\dot{\mathcal{V}}_2(t) + 2\alpha\mathcal{V}_2(t)\right\} \le \mu_q\kappa_q s_{\min}^2. \tag{3.11}$$

To combine the estimates obtained on the two subintervals, introduce the piecewise functional

$$\mathcal{V}(t) = \begin{cases} \mathcal{V}_1(t), & t \in \mathcal{T}_k^{(1)}, \\ \mathcal{V}_2(t), & t \in \mathcal{T}_k^{(2)}. \end{cases}$$

At $t = t_k + T_{\min}$, the multiplier $T_{\min} - \Delta(t)$ becomes zero. The terms $\mathcal{V}_1^S(t)$ and $\mathcal{V}_1^H(t)$ therefore vanish. Consequently,

$$\mathcal{V}_1((t_k + T_{\min})^-) = x^{\mathrm{T}}(t_k + T_{\min})\mathbf{P}x(t_k + T_{\min}) = \mathcal{V}_2(t_k + T_{\min}).$$

At t_{k+1}, the first-subinterval functional for the next interevent interval is reinitialized with elapsed time measured from t_{k+1}; hence, its elapsed-time argument is zero. Its integral term vanishes. The identity

$$\begin{bmatrix} \mathbf{I} & \mathbf{I} \end{bmatrix}\mathbf{H}_0\begin{bmatrix} \mathbf{I} & \mathbf{I} \end{bmatrix}^{\mathrm{T}} = 0$$

also removes its looped-functional term. The functional values satisfy

$$\mathcal{V}_1(t_{k+1}) = x^{\mathrm{T}}(t_{k+1})\mathbf{P}x(t_{k+1}) = \mathcal{V}_2((t_{k+1})^-).$$

These equalities establish continuity at the switching instants. Combining (3.8) and (3.11) yields

$$\frac{d}{dt}\mathbb{E}\{\mathcal{V}(t)\} + 2\alpha\mathbb{E}\{\mathcal{V}(t)\} \leq \mu_q\kappa_q s_{\min}^2 \tag{3.12}$$

for almost all $t \geq t_0$. Multiplying (3.12) by $e^{2\alpha t}$ and integrating over $[t_0, t]$ gives

$$\mathbb{E}\{\mathcal{V}(t)\} \leq e^{-2\alpha(t-t_0)}\mathbb{E}\{\mathcal{V}(t_0)\} + \frac{\mu_q\kappa_q s_{\min}^2}{2\alpha}\left[1 - e^{-2\alpha(t-t_0)}\right]. \tag{3.13}$$

Using the convex-combination representation above and the definition of $\underline{c}$ in Theorem 1, one has

$$\mathcal{V}_1^P(t) + \mathcal{V}_1^H(t) \geq \frac{\Delta(t)}{T_{\min}}\lambda_{\min}(\mathbf{P})\|x(t)\|^2 + \frac{T_{\min} - \Delta(t)}{T_{\min}}\lambda_{\min}\left(\begin{bmatrix}\mathbf{P} & 0\\ 0 & 0\end{bmatrix} + T_{\min}\mathbf{H}_0\right)\|x(t)\|^2 \geq \underline{c}\|x(t)\|^2.$$

Because $\mathcal{V}_1^S(t) \geq 0$,

$$\mathcal{V}_1(t) \geq \underline{c}\|x(t)\|^2.$$

For the second subinterval,

$$\mathcal{V}_2(t) = x^{\mathrm{T}}(t)\mathbf{P}x(t) \geq \lambda_{\min}(\mathbf{P})\|x(t)\|^2 \geq \underline{c}\|x(t)\|^2.$$

Hence,

$$\underline{c}\|x(t)\|^2 \leq \mathcal{V}(t) \tag{3.14}$$

holds on both subintervals.

At the initial event instant,

$$\mathcal{V}(t_0) = x^{\mathrm{T}}(t_0)\mathbf{P}x(t_0),$$

and therefore,

$$\mathbb{E}\{\mathcal{V}(t_0)\} \leq \lambda_{\max}(\mathbf{P})\mathbb{E}\{\|x(t_0)\|^2\}. \tag{3.15}$$

Substituting (3.15) into (3.13) and using (3.14) gives

$$\mathbb{E}\{\|x(t)\|^2\} \leq \frac{\lambda_{\max}(\mathbf{P})}{\underline{c}}e^{-2\alpha(t-t_0)}\mathbb{E}\{\|x(t_0)\|^2\} + \frac{\mu_q\kappa_q s_{\min}^2}{2\alpha\underline{c}}.$$

This inequality satisfies Definition 1 with

$$c_1 = \frac{\lambda_{\max}(\mathbf{P})}{\underline{c}},\ c_2 = 2\alpha,\ c_3 = \frac{\mu_q\kappa_q s_{\min}^2}{2\alpha\underline{c}}.$$

The closed-loop system under Bernoulli packet losses therefore satisfies MSEUB. Its ultimate bound satisfies

$$\limsup_{t\to\infty}\mathbb{E}\{\|x(t)\|^2\} \leq \frac{\mu_q\kappa_q s_{\min}^2}{2\alpha\underline{c}}.$$

□

Remark 4. *The ultimate bound in Theorem 1 is affected by the finite-bit reconstruction parameters b_z and $s_{\min}$. According to Lemma 1, increasing b_z reduces the reconstruction-related term through κ_q but increases the payload length $n_y b_z$. The influence of $s_{\min}$ follows from* (2.10) *and* (2.12). *When $\|y(t_k)\|_\infty < s_{\min}$, decreasing $s_{\min}$ provides finer resolution near the origin and reduces the $s_{\min}^2$-dependent residual term in the MSEUB bound, whereas increasing $s_{\min}$ enlarges the minimum physical quantization range at the expense of a coarser resolution. When $\|y(t_k)\|_\infty \geq s_{\min}$, the scale is determined by the current output magnitude, so $s_{\min}$ no longer affects the instantaneous quantization range. Moreover,* (2.10) *ensures $s(t_k) \geq \|y(t_k)\|_\infty$, so varying $s_{\min}$ does not introduce quantizer overflow.*

The packet-reception probability p_s enters the LMI conditions and therefore influences the feasible controller and the resulting MSEUB bound under unreliable transmissions. In addition, η affects the event sequence and N_{tx}, and $T_{\min}$ constrains the admissible transmission frequency. Hence, the MSEUB bound characterizes closed-loop regulation under packet losses and finite-bit reconstruction, whereas N_{tx}, $n_y b_z$, and $T_{\min}$ characterize sensor-to-controller communication usage and real-time requirements. These quantities jointly describe the tradeoff between closed-loop performance, communication reliability, and network resource usage [15, 18].

Remark 5. *The conditions in Theorem 1 contain coupling terms between the Lyapunov matrices and controller variables. By further processing these terms, Theorem 2 provides a solver-compatible LMI reformulation, following a strategy similar to that in [42].*

Theorem 2. *Assume that the packet-reception process satisfies* (3.1) *and that the encoding–decoding scheme satisfies the conditions of Lemma 1. For given $b_z \geq 2$; $s_{\min} > 0$; and $\varepsilon_0, T_{\min}, \alpha, \tau_1, \tau_2, \rho_1, \rho_2 > 0$, define $q_z = 2^{b_z}$ and $\kappa_q = n_y/q_z^2$. If there exist $\mathbf{P} = \mathbf{P}^{\mathrm{T}} > 0$ and $\mathbf{S} = \mathbf{S}^{\mathrm{T}} > 0$ in $\mathbb{R}^{n_x \times n_x}$; $\mathbf{W} = \mathbf{W}^{\mathrm{T}} > 0$ in $\mathbb{R}^{n_y \times n_y}$; $\mathbf{K} \in \mathbb{R}^{n_u \times n_y}$, $\mathbf{Z}, \mathbf{Z}_1, \mathbf{N}_3 \in \mathbb{R}^{n_x \times n_x}$, $\mathbf{M}_i, \mathbf{F}_i, \mathbf{N}_i \in \mathbb{R}^{n_x \times n_x}$ for $i \in \{1, 2\}$; and $\mu_q > 0$ such that* (3.3a) *and the following matrix inequalities hold:*

$$\widehat{\mathbf{\Phi}}_0^{\sigma} = \begin{bmatrix} \mathbf{\Phi}_{11}(0) & \mathbf{\Phi}_{12}(0) & \bar{\mathbf{\Phi}}_{13}(0) & 0 & \tau_1\mathbf{M}_1^{\mathrm{T}} & 0 & \mathbf{M}_1^{\mathrm{T}} \\ * & \mathbf{\Phi}_{22}(0) & \bar{\mathbf{\Phi}}_{23}(0) & 0 & \tau_1\mathbf{M}_2^{\mathrm{T}} & 0 & \mathbf{M}_2^{\mathrm{T}} \\ * & * & \mathbf{\Phi}_{33}^{q}(0) & 0 & 0 & \sqrt{\nu_s}(\mathbf{BKC})^{\mathrm{T}} & -\rho_1 p_s(\mathbf{BKC})^{\mathrm{T}} \\ * & * & * & -\mu_q\mathbf{I}_{n_y} & 0 & \sqrt{\nu_s}(\mathbf{BK})^{\mathrm{T}} & -\rho_1 p_s(\mathbf{BK})^{\mathrm{T}} \\ * & * & * & * & -\tau_1\mathbf{I}_{n_x} & 0 & 0 \\ * & * & * & * & * & -\tau_1\mathbf{I}_{n_x} & 0 \\ * & * & * & * & * & * & -2\rho_1\mathbf{I}_{n_x} \end{bmatrix} < 0, \tag{3.16a}$$

$$\widehat{\mathbf{\Phi}}_{T_{\min}}^{\sigma} = \begin{bmatrix} \mathbf{\Phi}_{11}(T_{\min}) & \mathbf{\Phi}_{12}(T_{\min}) & \bar{\mathbf{\Phi}}_{13}(T_{\min}) & T_{\min}\mathbf{N}_1 & 0 & \tau_1\mathbf{M}_1^{\mathrm{T}} & 0 & \mathbf{M}_1^{\mathrm{T}} \\ * & \mathbf{\Phi}_{22}(T_{\min}) & \bar{\mathbf{\Phi}}_{23}(T_{\min}) & T_{\min}\mathbf{N}_2 & 0 & \tau_1\mathbf{M}_2^{\mathrm{T}} & 0 & \mathbf{M}_2^{\mathrm{T}} \\ * & * & \mathbf{\Phi}_{33}^{q}(T_{\min}) & T_{\min}\mathbf{N}_3 & 0 & 0 & \sqrt{\nu_s}(\mathbf{BKC})^{\mathrm{T}} & -\rho_1 p_s(\mathbf{BKC})^{\mathrm{T}} \\ * & * & * & -T_{\min}e^{-2\alpha T_{\min}}\mathbf{S} & 0 & 0 & 0 & 0 \\ * & * & * & * & -\mu_q\mathbf{I}_{n_y} & 0 & \sqrt{\nu_s}(\mathbf{BK})^{\mathrm{T}} & -\rho_1 p_s(\mathbf{BK})^{\mathrm{T}} \\ * & * & * & * & * & -\tau_1\mathbf{I}_{n_x} & 0 & 0 \\ * & * & * & * & * & * & -\tau_1\mathbf{I}_{n_x} & 0 \\ * & * & * & * & * & * & * & -2\rho_1\mathbf{I}_{n_x} \end{bmatrix} < 0, \tag{3.16b}$$

$$\widehat{\boldsymbol{\Theta}}^{\sigma} = \begin{bmatrix} \bar{\boldsymbol{\Theta}}_{11}^{q} & \bar{\boldsymbol{\Theta}}_{12} & \bar{\boldsymbol{\Theta}}_{13}^{q} & 0 & \tau_2\mathbf{F}_1^{\mathrm{T}} & \sqrt{\nu_s}(\mathbf{BKC})^{\mathrm{T}} & \mathbf{F}_1^{\mathrm{T}} - \rho_2 p_s(\mathbf{BKC})^{\mathrm{T}} \\ * & -\mathrm{He}(\mathbf{F}_2) & 0 & 0 & \tau_2\mathbf{F}_2^{\mathrm{T}} & 0 & \mathbf{F}_2^{\mathrm{T}} \\ * & * & \bar{\boldsymbol{\Theta}}_{33}^{q} & 0 & 0 & \sqrt{\nu_s}(\mathbf{BK})^{\mathrm{T}} & -\rho_2 p_s(\mathbf{BK})^{\mathrm{T}} \\ * & * & * & -\mu_q\mathbf{I}_{n_y} & 0 & \sqrt{\nu_s}(\mathbf{BK})^{\mathrm{T}} & -\rho_2 p_s(\mathbf{BK})^{\mathrm{T}} \\ * & * & * & * & -\tau_2\mathbf{I}_{n_x} & 0 & 0 \\ * & * & * & * & * & -\tau_2\mathbf{I}_{n_x} & 0 \\ * & * & * & * & * & * & -2\rho_2\mathbf{I}_{n_x} \end{bmatrix} \prec 0, \tag{3.16c}$$

where

$$\begin{aligned} \bar{\boldsymbol{\Phi}}_{13}(\Delta(t)) &= \mathbf{N}_1 - \mathbf{N}_3^{\mathrm{T}} + [1 - 2\alpha(T_{\min} - \Delta(t))](\mathbf{Z} - \mathbf{Z}_1), \quad & \bar{\boldsymbol{\Phi}}_{23}(\Delta(t)) &= \mathbf{N}_2 - (T_{\min} - \Delta(t))(\mathbf{Z} - \mathbf{Z}_1), \\ \bar{\boldsymbol{\Theta}}_{11}^{q} &= 2\alpha\mathbf{P} + \varepsilon_0\mathbf{C}^{\mathrm{T}}\mathbf{W}\mathbf{C} + \mu_q\kappa_q\mathbf{C}^{\mathrm{T}}\mathbf{C} + \mathrm{He}(\mathbf{F}_1^{\mathrm{T}}\mathbf{A}), & \bar{\boldsymbol{\Theta}}_{12} &= \mathbf{P} + \mathbf{A}^{\mathrm{T}}\mathbf{F}_2 - \mathbf{F}_1^{\mathrm{T}}, \\ \bar{\boldsymbol{\Theta}}_{13}^{q} &= \mu_q\kappa_q\mathbf{C}^{\mathrm{T}}, & \bar{\boldsymbol{\Theta}}_{33}^{q} &= -\mathbf{W} + \mu_q\kappa_q\mathbf{I}_{n_y}, \end{aligned}$$

then the closed-loop system in (2.20) *and* (2.22) *under Bernoulli packet losses satisfies MSEUB and*

$$\limsup_{t\to\infty} \mathbb{E}\{\|x(t)\|^2\} \leq \frac{\mu_q\kappa_q s_{\min}^2}{2\alpha\underline{c}}.$$

Proof. Let $\boldsymbol{\Lambda}_0$ denote the leading principal submatrix of $\widehat{\boldsymbol{\Phi}}_0^{\sigma}$ obtained by deleting its last block row and column. Then, (3.16a) can be written as

$$\widehat{\boldsymbol{\Phi}}_0^{\sigma} = \begin{bmatrix} \boldsymbol{\Lambda}_0 & \mathbf{U}_0 + \rho_1\mathbf{V}_0 \\ * & -2\rho_1\mathbf{I}_{n_x} \end{bmatrix} \prec 0,$$

where

$$\mathbf{U}_0 = \begin{bmatrix} \mathbf{M}_1 & \mathbf{M}_2 & 0 & 0 & 0 & 0 \end{bmatrix}^{\mathrm{T}}, \ \mathbf{V}_0 = \begin{bmatrix} 0 & 0 & -p_s\mathbf{BKC} & -p_s\mathbf{BK} & 0 & 0 \end{bmatrix}^{\mathrm{T}}.$$

This matrix has the form of Lemma 2 with $\mathbf{R} = \mathbf{I}_{n_x}$, as $-\rho_1\mathbf{R} - \rho_1\mathbf{R}^{\mathrm{T}} = -2\rho_1\mathbf{I}_{n_x}$. Hence, (3.16a) guarantees

$$\boldsymbol{\Lambda}_0 + \mathrm{He}(\mathbf{U}_0\mathbf{V}_0^{\mathrm{T}}) \prec 0.$$

The term $\mathrm{He}(\mathbf{U}_0\mathbf{V}_0^{\mathrm{T}})$ introduces the blocks $-p_s\mathbf{M}_i^{\mathrm{T}}\mathbf{BKC}$ and $-p_s\mathbf{M}_i^{\mathrm{T}}\mathbf{BK}$ for $i \in \{1, 2\}$. Together with the definitions of $\bar{\boldsymbol{\Phi}}_{13}(0)$ and $\bar{\boldsymbol{\Phi}}_{23}(0)$, the resulting matrix satisfies

$$\boldsymbol{\Lambda}_0 + \mathrm{He}(\mathbf{U}_0\mathbf{V}_0^{\mathrm{T}}) = \boldsymbol{\Phi}_0^{\sigma}.$$

Therefore, (3.16a) guarantees $\boldsymbol{\Phi}_0^{\sigma} \prec 0$ in (3.3b).

Let $\boldsymbol{\Lambda}_{T_{\min}}$ denote the leading principal submatrix of $\widehat{\boldsymbol{\Phi}}_{T_{\min}}^{\sigma}$ obtained by deleting its last block row and column. Inequality (3.16b) can be written as

$$\widehat{\boldsymbol{\Phi}}_{T_{\min}}^{\sigma} = \begin{bmatrix} \boldsymbol{\Lambda}_{T_{\min}} & \mathbf{U}_{T_{\min}} + \rho_1\mathbf{V}_{T_{\min}} \\ * & -2\rho_1\mathbf{I}_{n_x} \end{bmatrix} \prec 0,$$

where

$$\mathbf{U}_{T_{\min}} = \begin{bmatrix} \mathbf{M}_1 & \mathbf{M}_2 & 0 & 0 & 0 & 0 & 0 \end{bmatrix}^{\mathrm{T}}, \ \mathbf{V}_{T_{\min}} = \begin{bmatrix} 0 & 0 & -p_s\mathbf{BKC} & 0 & -p_s\mathbf{BK} & 0 & 0 \end{bmatrix}^{\mathrm{T}}.$$

Applying Lemma 2 with $\mathbf{R} = \mathbf{I}_{n_x}$ shows that (3.16b) guarantees

$$\mathbf{\Lambda}_{T_{\min}} + \mathrm{He}\left(\mathbf{U}_{T_{\min}}\mathbf{V}_{T_{\min}}^{\mathrm{T}}\right) \prec 0.$$

The added term recovers the controller-dependent blocks in $\mathbf{\Phi}_{13}(T_{\min})$ and $\mathbf{\Phi}_{23}(T_{\min})$, together with the corresponding blocks associated with $\mathbf{BK}$. Therefore,

$$\mathbf{\Lambda}_{T_{\min}} + \mathrm{He}\left(\mathbf{U}_{T_{\min}}\mathbf{V}_{T_{\min}}^{\mathrm{T}}\right) = \mathbf{\Phi}_{T_{\min}}^{\sigma},$$

and (3.16b) guarantees $\mathbf{\Phi}_{T_{\min}}^{\sigma} \prec 0$ in (3.3c).

Finally, let $\mathbf{\Lambda}_{\Theta}$ denote the leading principal submatrix of $\widehat{\mathbf{\Theta}}^{\sigma}$ obtained by deleting its last block row and column. Inequality (3.16c) can be written as

$$\widehat{\mathbf{\Theta}}^{\sigma} = \begin{bmatrix} \mathbf{\Lambda}_{\Theta} & \mathbf{U}_{\Theta} + \rho_2 \mathbf{V}_{\Theta} \\ * & -2\rho_2 \mathbf{I}_{n_x} \end{bmatrix} \prec 0,$$

where

$$\mathbf{U}_{\Theta} = \begin{bmatrix} \mathbf{F}_1 & \mathbf{F}_2 & 0 & 0 & 0 & 0 \end{bmatrix}^{\mathrm{T}}, \ \mathbf{V}_{\Theta} = \begin{bmatrix} -p_s\mathbf{BKC} & 0 & -p_s\mathbf{BK} & -p_s\mathbf{BK} & 0 & 0 \end{bmatrix}^{\mathrm{T}}.$$

Lemma 2 with $\mathbf{R} = \mathbf{I}_{n_x}$ shows that (3.16c) guarantees

$$\mathbf{\Lambda}_{\Theta} + \mathrm{He}(\mathbf{U}_{\Theta}\mathbf{V}_{\Theta}^{\mathrm{T}}) \prec 0.$$

The term $\mathrm{He}(\mathbf{U}_{\Theta}\mathbf{V}_{\Theta}^{\mathrm{T}})$ recovers $\mathrm{He}(-p_s\mathbf{F}_1^{\mathrm{T}}\mathbf{BKC})$ in the $(1,1)$ block, $-p_s(\mathbf{BKC})^{\mathrm{T}}\mathbf{F}_2$ in the $(1,2)$ block, and the products $-p_s\mathbf{F}_i^{\mathrm{T}}\mathbf{BK}$ associated with $e_y(t)$ and $e_q(t_k)$. Hence,

$$\mathbf{\Lambda}_{\Theta} + \mathrm{He}(\mathbf{U}_{\Theta}\mathbf{V}_{\Theta}^{\mathrm{T}}) = \mathbf{\Theta}^{\sigma}.$$

The terms involving $\mu_q\kappa_q$ are already contained in $\mathbf{\Lambda}_{\Theta}$ and are not affected by the slack-matrix transformation. Therefore, (3.16c) guarantees $\mathbf{\Theta}^{\sigma} \prec 0$ in (3.3d).

Thus, (3.3a), $\mathbf{\Phi}_0^{\sigma} \prec 0$, $\mathbf{\Phi}_{T_{\min}}^{\sigma} \prec 0$, and $\mathbf{\Theta}^{\sigma} \prec 0$ are all satisfied. Therefore, Theorem 1 applies, which establishes the MSEUB property together with the stated ultimate bound. □

Remark 6. *From a computational perspective, for fixed scalar design parameters, Theorem 2 contains* $10n_x^2 + n_x + n_y(n_y+1)/2 + n_u n_y + 1$ *scalar decision variables, and the principal LMI orders are* $2n_x$, $6n_x + n_y$, $7n_x + n_y$, *and* $5n_x + 2n_y$. *Thus, the number of decision variables grows quadratically with the state dimension, whereas the orders of the principal semidefinite constraints grow linearly with the state and output dimensions. For the numerical example with* $n_x = 2$, $n_y = 2$, *and* $n_u = 1$, *the formulation contains 48 scalar decision variables, with LMI orders* 4, 14, 16, *and* 14. *The resulting semidefinite program is computationally modest for the considered example, although sparsity exploitation or decomposition techniques may improve scalability for higher-dimensional systems.*

4. Numerical example and simulation results

4.1. Simulation setup and LMI feasibility

Numerical simulations are conducted to evaluate the closed-loop control performance, communication usage, and finite-bit reconstruction performance of the proposed framework. The

NCS plant considered in the simulations is

$$\mathbf{A} = \begin{bmatrix} 0 & 1 \\ 0.08 & -0.8 \end{bmatrix}, \ \mathbf{B} = \begin{bmatrix} 0 \\ 1 \end{bmatrix}, \ \mathbf{C} = \mathbf{I}_2. \tag{4.1}$$

All simulations are carried out in MATLAB R2024a with an integration step of 0.001 s. Let $T_f = 60$ s denote the simulation horizon, and let the initial state be $x(0) = [1.2, -1.2]^{\mathrm{T}}$. Unless otherwise specified, $T_{\min} = 0.1$, $\varepsilon_0 = 0.05$, $\eta = 0.25$, $s_{\min} = 0.01$, and $b_z = 12$. For the LMI design, $\alpha = 0.01$, $\rho_1 = 1$, $\rho_2 = 10$, and $\tau_1 = \tau_2 = 1$.

Using Theorem 2, the output-feedback gains are obtained with YALMIP and MOSEK. For $p_{\text{loss}} = 0.1$, 0.2, and 0.3, the corresponding gains are

$$\mathbf{K}_{0.1} = [0.346 \quad -0.034], \ \mathbf{K}_{0.2} = [0.878 \ \ 0.642], \ \mathbf{K}_{0.3} = [2.818 \ \ 3.078],$$

respectively. The corresponding triggering weight matrices used by PLAETM are

$$\mathbf{W}_{0.1} = \begin{bmatrix} 0.0907 & -0.0088 \\ -0.0088 & 0.0016 \end{bmatrix}, \ \mathbf{W}_{0.2} = \begin{bmatrix} 0.5930 & 0.4322 \\ 0.4322 & 0.3180 \end{bmatrix}, \ \mathbf{W}_{0.3} = \begin{bmatrix} 4.0420 & 4.4130 \\ 4.4130 & 4.8219 \end{bmatrix},$$

respectively.

To examine the numerical feasibility of the LMI conditions with respect to the packet-loss probability, $b_z = 12$ is fixed, and p_{loss} is further increased from 0.30 to 0.35; all other design parameters are kept unchanged. Feasible solutions of Theorem 2 are obtained at $p_{\text{loss}} = 0.31$ and 0.32, yielding

$$\mathbf{K}_{0.31} = [2.999 \ \ 3.348], \qquad \mathbf{K}_{0.32} = [3.084 \ \ 3.486],$$

respectively. No feasible solution is obtained at $p_{\text{loss}} = 0.33$, 0.34, or 0.35. Hence, $p_{\text{loss}} = 0.32$ is the largest tested packet-loss probability for which a feasible solution of Theorem 2 is obtained.

The influence of the finite-bit resolution on LMI feasibility is further examined by fixing $p_{\text{loss}} = 0.30$ and decreasing b_z. Because the result for $b_z = 12$ has already been given above, Table 1 reports the feasible solutions for $b_z = 11$ to 5. All remaining design parameters are kept unchanged, and the controller gain at each test point is obtained directly from Theorem 2. Let $\mathcal{X}^\star$ collect the decision-variable values returned by MOSEK. For each LMI, define the corresponding sign-normalized residual matrix $\mathcal{L}_i(\mathcal{X}^\star)$, $i = 1, \ldots, N_{\text{LMI}}$, such that strict feasibility requires $\mathcal{L}_i(\mathcal{X}^\star) \succ 0$; the residual of a negative-definite LMI is multiplied by -1. The post-solution LMI margin is defined as

$$\delta_{\text{LMI}} := \min_{1 \le i \le N_{\text{LMI}}} \lambda_{\min}(\mathcal{L}_i(\mathcal{X}^\star)).$$

Thus, $\delta_{\text{LMI}} > 0$ indicates positive eigenvalue clearance for every evaluated LMI at the returned numerical solution. This post-solution feasibility measure is computed separately from the MOSEK stopping tolerances. Feasible solutions are obtained for all tested bit resolutions from $b_z = 11$ down to $b_z = 5$. Together with the result for $b_z = 12$, feasible solutions of Theorem 2 are obtained over the tested range $5 \le b_z \le 12$ at $p_{\text{loss}} = 0.30$. No feasible solution is obtained for $b_z = 4$, 3, or 2. Thus, $b_z = 5$ is the smallest tested bit resolution for which a feasible solution of Theorem 2 is obtained.

Table 1. Controller gains and LMI margins versus bit resolution at $p_{\text{loss}} = 0.30$.

b_z	11	10	9	8	7	6	5
$\mathbf{K}$	[3.054, 3.354]	[3.157, 3.486]	[3.260, 3.618]	[3.333, 3.756]	[3.432, 3.894]	[3.531, 4.032]	[3.453, 3.894]
δ_{LMI}	1.9404×10^{-3}	2.0090×10^{-3}	2.0522×10^{-3}	2.0460×10^{-3}	1.9318×10^{-3}	1.5361×10^{-3}	2.7631×10^{-4}

Remark 7. *To obtain solver-compatible LMI conditions for controller synthesis, Theorem 2 employs a slack-matrix treatment to decouple the coupling terms between the Lyapunov matrices and the controller variables in Theorem 1. Because Theorem 2 provides sufficient conditions, this reformulation may introduce additional conservatism. Infeasibility at a particular parameter setting is specific to the present sufficient LMI conditions; a stabilizing controller may exist outside the certified feasible region. Less conservative slack-variable treatments and advanced looped-functional constructions [32, 43] may enlarge this region.*

4.2. Closed-loop and communication performance

For a consistent comparison, all four mechanisms use the same plant, initial state, integration step, simulation horizon, packet-loss probability, finite-bit encoding setting, and corresponding feedback gain. Within each Monte Carlo run, the same packet-loss realization is used for all four mechanisms. The nominal threshold level 0.05 is used whenever a directly comparable threshold is present. The baseline-specific tuning parameters remain fixed across all packet-loss conditions, and the Monte Carlo runs are conducted without runwise retuning. For each packet-loss probability, the corresponding feedback gain and PLAETM triggering weight matrix are synthesized once and then fixed throughout the Monte Carlo runs. Full-space optimization of the baseline parameters lies outside the comparison protocol. The reported results therefore provide controlled comparisons among the specified adapted implementations. Alternative baseline tuning may change the quantitative communication–regulation trade-offs and rankings. Performance variations across different p_{loss} values reflect the combined effects of the packet-loss condition and the corresponding LMI-based design.

For parameters having direct counterparts in PLAETM, the same settings are retained, with the time scales referenced to $T_{\min}$ and the triggering thresholds to ε_0. The SCP baseline adopts the multiple-probability sampling structure in [19], with intertransmission periods $T_{\min}$, $2T_{\min}$, and $3T_{\min}$ selected with probabilities 0.55, 0.30, and 0.15, respectively. The TDSETCM baseline follows the threshold-based triggering structure in [29] with the fixed threshold ε_0. The DPETCM baseline follows the periodic dynamic triggering structure in [30], where the triggering condition is evaluated every $T_{\min}$ using the threshold ε_0. Its dynamic variable is initialized by $\chi^{\mathrm{DP}}(0) = 0.08$, with $\lambda_\chi^{\mathrm{DP}} = 0.25$, $\sigma_y^{\mathrm{DP}} = 0.20$, $\sigma_e^{\mathrm{DP}} = 0.40$, and $\chi_{\max}^{\mathrm{DP}} = 0.25$, and is updated using the same simulation step with projection onto $[0, \chi_{\max}^{\mathrm{DP}}]$.

Figure 2 presents the uncontrolled open-loop response and the closed-loop realization of the proposed PLAETM–SNEDM framework at $p_{\mathrm{loss}} = 0.3$. The upper panel shows that the open-loop states exhibit a divergent tendency. In the lower panel, both state components enter and remain in a neighborhood of the origin despite random packet losses and finite-bit output reconstruction. These responses illustrate closed-loop state regulation under the considered communication condition.

A finite-horizon numerical check is performed for the theoretical ultimate bound. Let $x_j(t)$ denote the state trajectory in the jth Monte Carlo run. The empirical terminal mean-square state measure over the $N_{\mathrm{MC}} = 30$ independent PLAETM runs is defined as

$$\widehat{U}_f = \frac{1}{N_{\mathrm{MC}}} \sum_{j=1}^{N_{\mathrm{MC}}} \left\| x_j(T_f) \right\|^2 . \tag{4.2}$$

Let U_{th} denote the theoretical ultimate bound given in Theorem 1. Table 2 compares $\widehat{U}_f$ with U_{th} under the three packet-loss probabilities. In all tested cases, the empirical terminal mean-square state

measure remains below the corresponding theoretical bound. The finite-horizon Monte Carlo results are therefore consistent with the mean-square ultimate-bound estimate in Theorem 1.

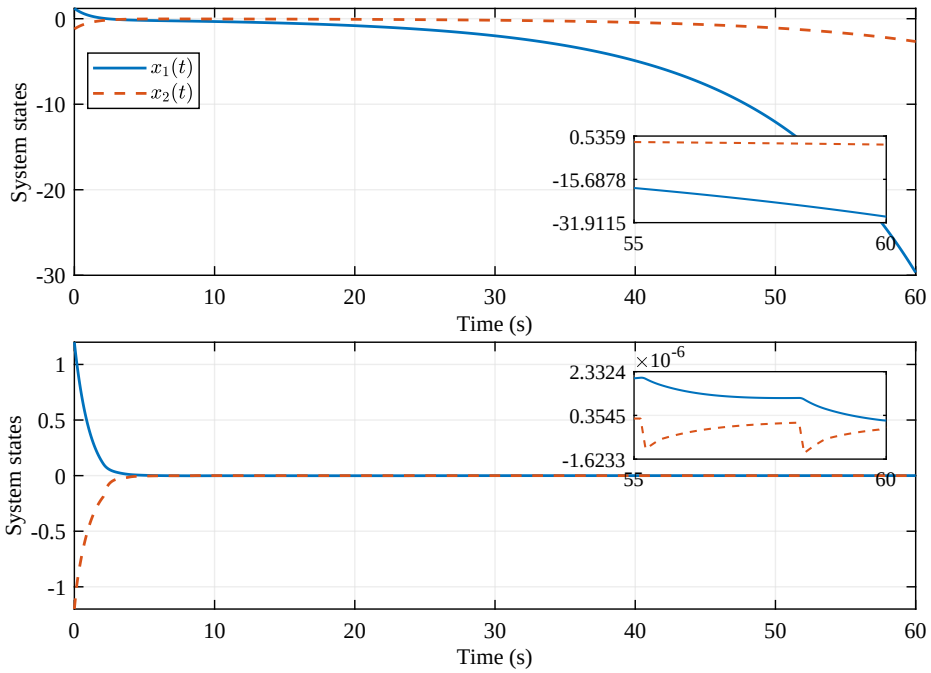


Figure 2. Open-loop and PLAETM–SNEDM closed-loop state responses at $p_{\text{loss}} = 0.3$, shown in the upper and lower panels, respectively.

Table 2. Comparison of empirical and theoretical ultimate bounds.

p_{loss}	$\widehat{U}_f$	U_{th}	$\widehat{U}_f/U_{\text{th}}$
0.1	6.201×10^{-14}	1.292×10^{-9}	4.80×10^{-5}
0.2	7.596×10^{-9}	8.071×10^{-9}	0.9412
0.3	2.016×10^{-9}	4.974×10^{-7}	0.00405

For the packet-loss realization at $p_{\text{loss}} = 0.3$, Figure 3 compares the closed-loop responses of the four mechanisms. To quantitatively evaluate communication usage and closed-loop performance, 30 independent runs are conducted for each packet-loss probability. The quantity N_{tx} denotes the total number of sensor-to-controller transmission attempts, including both successfully received and lost packets, and is reported as mean ± standard deviation. The N_{tx}-based comparison is restricted to utilization of the sensor-to-controller data link; total bidirectional network traffic lies outside the metric scope. The indices J_{IAE}, J_{RMS}, and J_u quantify the integral absolute error, root-mean-square state magnitude, and control effort, respectively, and are reported as mean values. They are defined as

$$J_{\text{IAE}} = \int_0^{T_f} \|x(t)\|_1 \, dt, \; J_{\text{RMS}} = \sqrt{\frac{1}{T_f} \int_0^{T_f} \|x(t)\|_2^2 \, dt}, \; J_u = \int_0^{T_f} \|u(t)\|_2^2 \, dt. \tag{4.3}$$

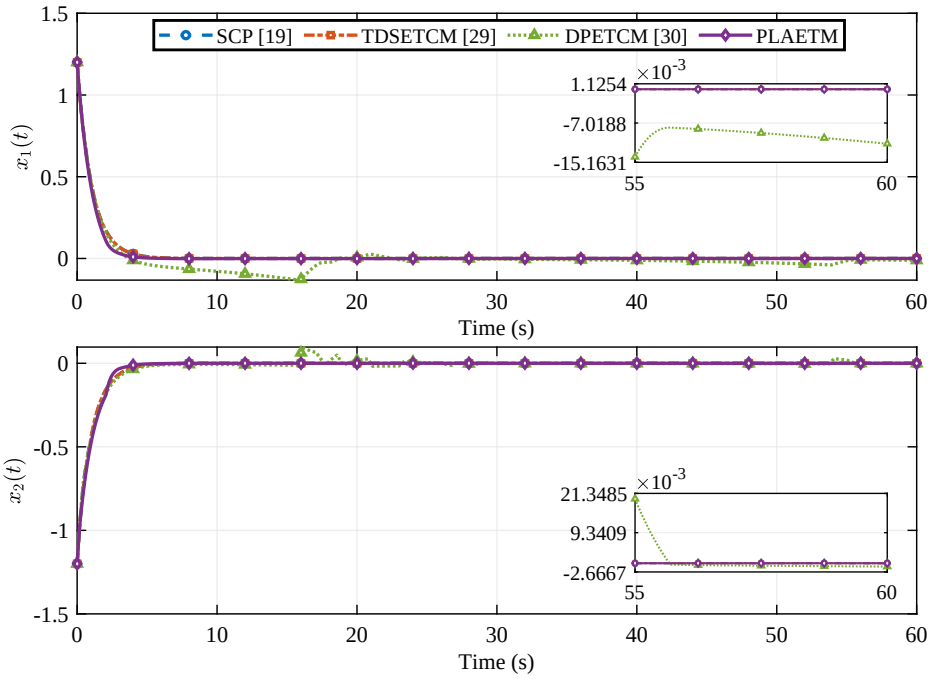


Figure 3. Closed-loop state responses under the four transmission mechanisms.

Table 3. Communication and closed-loop performance over 30 independent runs.

p_{loss}	Method	N_{tx}	J_{IAE}	J_{RMS}	J_u
0.1	SCP	372.37 ± 8.18	5.128	0.2044	0.1788
0.1	TDSETCM	239.53 ± 30.41	5.373	0.2102	0.1988
0.1	DPETCM	20.60 ± 1.83	9.201	0.2661	0.3823
0.1	PLAETM	201.47 ± 23.29	5.116	0.2040	0.1759
0.2	SCP	372.37 ± 8.18	2.588	0.1605	0.0498
0.2	TDSETCM	401.80 ± 33.07	2.769	0.1619	0.0570
0.2	DPETCM	22.90 ± 3.18	4.447	0.1820	0.1961
0.2	PLAETM	153.53 ± 71.28	3.197	0.1625	0.0472
0.3	SCP	372.37 ± 8.18	2.458	0.1550	0.0256
0.3	TDSETCM	319.97 ± 53.06	2.462	0.1550	0.0256
0.3	DPETCM	30.57 ± 7.08	6.607	0.1902	0.7605
0.3	PLAETM	103.33 ± 28.80	2.561	0.1555	0.0293

As summarized in Table 3, PLAETM requires fewer sensor-to-controller transmission attempts than SCP and TDSETCM under all three packet-loss conditions while maintaining comparable J_{RMS} values. Relative to SCP, PLAETM reduces the average number of transmission attempts by approximately 45.90%, 58.77%, and 72.25% for $p_{\text{loss}} = 0.1$, 0.2, and 0.3, respectively. The corresponding reductions relative to TDSETCM are approximately 15.89%, 61.79%, and 67.71%. Across the three packet-loss conditions, the absolute relative difference in J_{RMS} between PLAETM

and SCP remains below 1.25%, whereas that between PLAETM and TDSETCM remains below 2.95%. SCP transmits at each transmission instant determined by its prescribed sampling-period sequence. Because the same sampling-period setting is used under all three packet-loss conditions, its N_{tx} statistics remain unchanged.

DPETCM achieves the lowest N_{tx} under all three tested conditions and has larger J_{IAE}, J_{RMS}, and J_u. Relative to PLAETM, DPETCM reduces N_{tx} by approximately 89.78%, 85.08%, and 70.42% for $p_{\text{loss}} = 0.1$, 0.2, and 0.3, respectively. Relative to DPETCM, PLAETM reduces J_{RMS} by approximately 23.34%, 10.71%, and 18.24% under the same packet-loss conditions. These values locate DPETCM at a lower-communication, higher-regulation-error operating point. PLAETM uses more transmission attempts than DPETCM and maintains lower regulation indices while reducing transmission attempts relative to SCP and TDSETCM.

The communication counts in Table 3 exclude reception-status signaling, as specified in Section 2.2. A conservative overhead calculation assigns one reception-status bit to each PLAETM transmission attempt and zero such bits to SCP and TDSETCM. Because $n_y = 2$, and $b_z = 12$, each sensor packet contains $n_y b_z = 24$ bits, and the communication usage of PLAETM is therefore evaluated using $25N_{\text{tx}}$ bits. After including this additional bit, the communication usage of PLAETM remains approximately 43.64%, 57.05%, and 71.09% lower than that of SCP for $p_{\text{loss}} = 0.1$, 0.2, and 0.3, respectively. The corresponding reductions relative to TDSETCM are approximately 12.38%, 60.20%, and 66.36%.

4.3. Robustness and parameter sensitivity

An additional disturbance test at $p_{\text{loss}} = 0.3$ evaluates empirical robustness under challenging conditions. The controller, triggering parameters, and encoding settings remain unchanged from the disturbance-free case. In this stress test, the plant dynamics are augmented as

$$\dot{x}(t) = \mathbf{A}x(t) + \mathbf{B}u(t) + \zeta(t).$$

Three bounded disturbances are considered:

$$\zeta_1(t) = 0.020[\sin(0.50t),\ \cos(0.50t)]^{\mathrm{T}},$$

$$\zeta_2(t) = \begin{cases} [0.040,\ -0.030]^{\mathrm{T}}, & 20 \le t \le 30, \\ [0,\ 0]^{\mathrm{T}}, & \text{otherwise}, \end{cases}$$

$$\zeta_3(t) = 0.015[\sin(0.40t) + 0.5\sin(1.50t),\ \cos(0.60t) + 0.5\cos(1.80t)]^{\mathrm{T}}.$$

These cases serve as periodic, finite-duration, and multifrequency numerical stress tests, respectively. Figure 4 compares representative state responses under the three disturbances and the disturbance-free case. The periodic and multifrequency disturbances produce persistent small-amplitude oscillations after the initial transient. The finite-duration disturbance mainly affects the states during 20–30 s, and its influence decreases after the disturbance is removed. In all cases, both state components remain close to the origin without evident divergence.

Thirty independent runs are conducted for each case to account for variation among packet-loss realizations. Figure 5 reports the mean values and one-standard-deviation error bars. All three disturbances increase J_{IAE}, with only minor changes in J_{RMS}. The periodic disturbance yields the largest accumulated state deviation and control effort. The multifrequency disturbance results in the

largest number of transmission attempts. The finite-duration disturbance produces a smaller communication increase because it acts over a limited interval. Across these tests, the state trajectories remain close to the origin, and persistent perturbations increase communication and control effort.

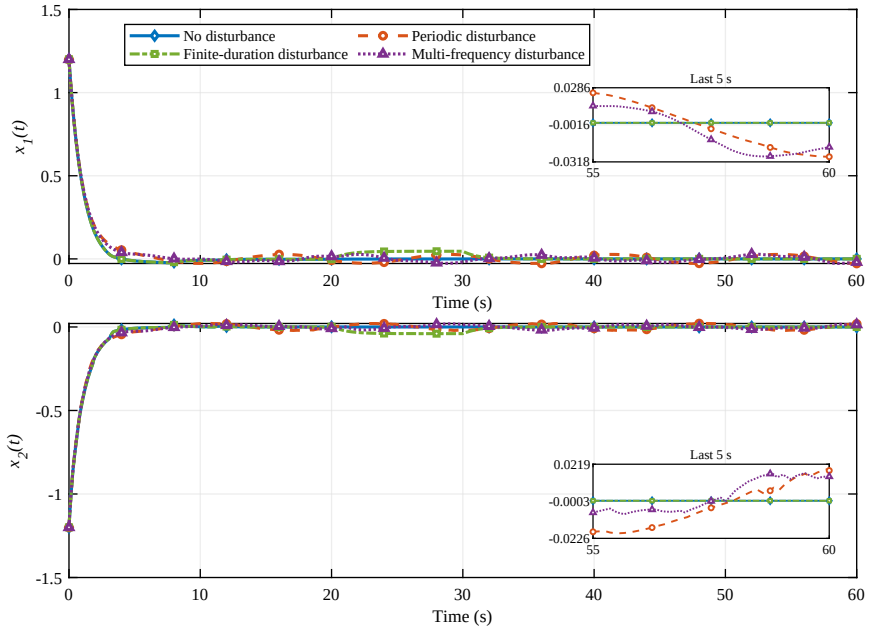


Figure 4. Closed-loop state responses under different external disturbances at $p_{\text{loss}} = 0.3$.

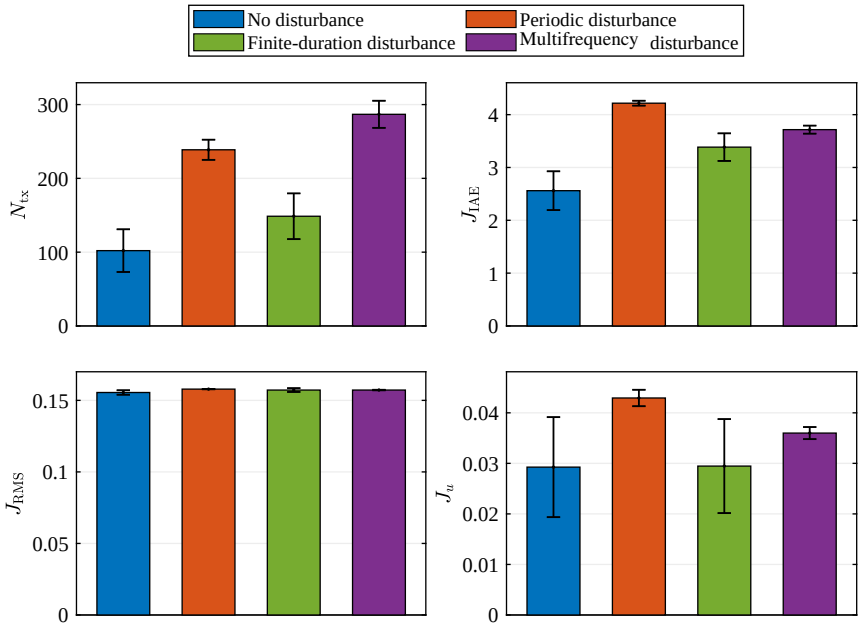


Figure 5. Closed-loop and communication performance under external disturbances.

The sensitivity of the PLAETM triggering parameters is examined under $p_{\text{loss}} = 0.3$ and $\varepsilon_0 = 0.05$. Each single-factor test uses a fixed packet-loss realization. As shown in Table 4, varying η noticeably changes N_{tx}, whereas J_{RMS} remains nearly unchanged. Because η adjusts the loss-dependent triggering threshold through the consecutive-loss counter, it changes the subsequent triggering sequence. This sequence also interacts with the closed-loop state evolution, producing the observed nonmonotonic variation in N_{tx}. Table 4 also shows that increasing $T_{\min}$ reduces the available triggering opportunities and generally decreases N_{tx}. Across both parameter sweeps, J_{RMS} changes only slightly despite the substantial variation in transmission counts.

Table 4. Sensitivity of the PLAETM triggering parameters.

η	0.25	0.75	1.50	2.50	4.00
N_{tx}	144	122	207	222	232
J_{RMS}	0.154965	0.154930	0.154926	0.154931	0.154939
$T_{\min}$	0.10	0.20	0.30	0.40	0.50
N_{tx}	144	124	94	70	71
J_{RMS}	0.154965	0.154964	0.155024	0.155113	0.155297

4.4. Finite-bit reconstruction comparison

The finite-bit reconstruction performance of SNEDM is compared with those of LSSQEDM [40] and DQZPEDM [39]. All methods use the same PLAETM output trajectory and $b_z = 12$ bits per output component. The trajectory is generated under $p_{\text{loss}} = 0.3$, $\varepsilon_0 = 0.05$, and $T_{\min} = 0.1$. Let $\mathcal{G} = \{t_\ell = \ell h : \ell = 0, \ldots, L\}$, where $h = 0.001$ s and $L = T_f/h$ denote the simulation grid. For each method $\mathcal{M}$, let $\widehat{y}_{\mathcal{M}}(t_\ell)$ denote the pointwise reconstruction of $y(t_\ell)$. The reported integral reconstruction error is

$$J_{\text{rec}}^{(\mathcal{M})} = \int_0^{T_f} \left\| \widehat{y}_{\mathcal{M}}(t) - y(t) \right\|_2 \, dt, \tag{4.4}$$

which is evaluated on $\mathcal{G}$ using the trapezoidal rule.

Let $a_{\mathcal{M}}(t_\ell)$ denote the half-range available to method $\mathcal{M}$ at t_ℓ. An overflow is recorded once at a grid point if any output component exceeds this range. Thus,

$$N_{\text{ov}}^{(\mathcal{M})} = \sum_{\ell=0}^{L} \mathbf{1}\left\{ \|y(t_\ell)\|_\infty > a_{\mathcal{M}}(t_\ell) \right\}, \tag{4.5}$$

where $\mathbf{1}\{\cdot\}$ denotes the indicator function. For LSSQ-small, LSSQ-nominal, and LSSQ-large, the constants $a_{\mathcal{M}} = 0.5$, 1.5, and 2.5 define the full quantization intervals $[-a_{\mathcal{M}}, a_{\mathcal{M}}]$. For all compared methods, each available quantization range is uniformly divided into 2^{b_z} intervals, and midpoint reconstruction is employed. The DQZPEDM half-range is initialized and updated according to [39] as

$$\begin{aligned} a_{\text{DQ}}(t_0) &= \max\{s_{\min}, 1.10\|y(t_0)\|_\infty\}, \\ a_{\text{DQ}}(t_\ell) &= \max\{s_{\min}, 0.985 a_{\text{DQ}}(t_{\ell-1}), 1.10\|y(t_{\ell-1})\|_\infty\}, \quad \ell \geq 1. \end{aligned}$$

The DQZPEDM encoding–decoding mechanism and dynamic-range update rule follow [39]. For a consistent reconstruction comparison, DQZPEDM, LSSQEDM, and SNEDM are evaluated using the

same output trajectory and the same bit length. SNEDM uses $a_{\mathrm{SN}}(t_\ell) = \max\{s_{\min}, \|y(t_\ell)\|_\infty\}$, so its normalized input remains within $[-1, 1]$ by construction.

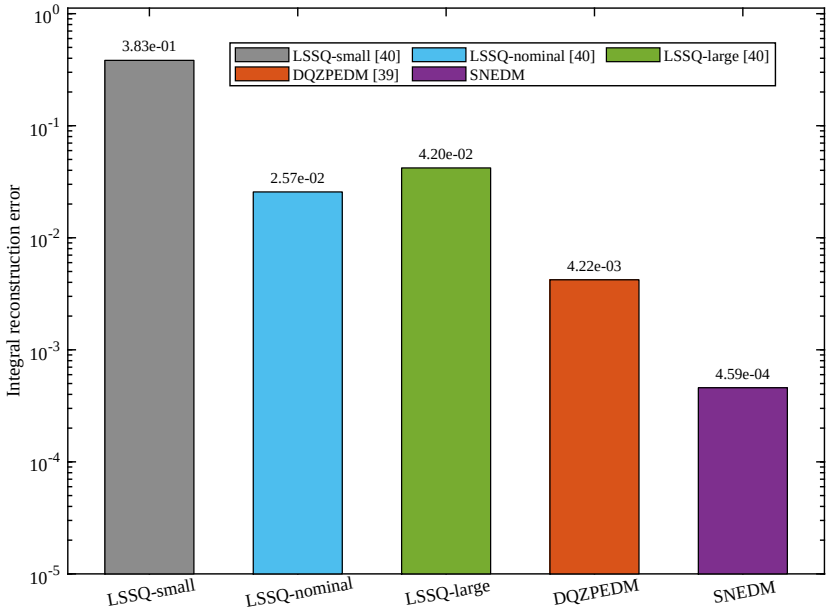


Figure 6. Integral reconstruction errors of the compared encoding–decoding methods under the same index length.

As shown in Figure 6, LSSQEDM exhibits a range–resolution tradeoff under a fixed bit length. According to (4.5), LSSQ-small produces $N_{\mathrm{ov}} = 939$, whereas $N_{\mathrm{ov}} = 0$ for LSSQ-nominal, LSSQ-large, DQZPEDM, and SNEDM. Increasing the prescribed range avoids overflow but enlarges the quantization interval. DQZPEDM alleviates this limitation by dynamically adjusting its quantization range and achieves a lower reconstruction error than the fixed-range cases considered here. By comparison, SNEDM maps each output sample into the prescribed normalized domain according to (2.10) and (2.11). It therefore avoids overflow without requiring a prescribed raw-output range and achieves the lowest J_{rec} among the compared methods.

5. Conclusions

This paper investigated the MSEUB problem for bandwidth-limited NCSes under Bernoulli packet losses and finite-bit output transmission. A unified framework combining PLAETM and SNEDM was developed. PLAETM adapts the triggering threshold according to consecutive packet losses. SNEDM maps triggered outputs into a bounded normalized domain for finite-bit transmission. A stochastic closed-loop model was established, and LMI conditions were derived for MSEUB and controller synthesis. Under the stated adapted implementations and parameter settings, PLAETM reduces sensor-to-controller transmission attempts relative to SCP and TDSETCM while retaining comparable regulation performance. DPETCM achieves lower transmission counts and larger regulation indices under the same conditions. Under the common trajectory and bit-length settings considered in the

numerical study, SNEDM achieves the lowest integral reconstruction error among the compared encoding–decoding methods and avoids overflow without requiring a prescribed raw-output range or recursive dynamic zooming. The present framework does not cover nonlinear plants, complex networks [44], learning-based control [45], temporally correlated or time-varying packet-loss channels, or prescribed-time mean-square analysis [46].

Use of generative-AI tools declaration

The authors declare they have not used Artificial Intelligence (AI) tools in the creation of this article.

Conflict of interest

The authors declare no conflicts of interest.

References

1. Y. Zhi, X. Liu, S. He, W. Lin, W. Chen, Adaptively event-triggered H_∞ control for networked autonomous aerial vehicles control systems under deception attacks, *IEEE Trans. Ind. Inf.*, **21** (2025), 3458–3465. https://doi.org/10.1109/TII.2025.3528560
2. Z. Wang, M. Bennis, Y. Zhou, Graph attention-based MADRL for access control and resource allocation in wireless networked control systems, *IEEE Trans. Wireless Commun.*, **23** (2024), 16076–16090. https://doi.org/10.1109/TWC.2024.3436906
3. S. Sun, C. Jia, F. Han, Consensus of multi-agent system with disturbance based on dynamical event-triggered control, *Electron. Res. Arch.*, **34** (2026), 2303–2320. https://doi.org/10.3934/era.2026104
4. X. Jiang, J. Li, B. Li, Y. Wang, T. Huang, Output tracking and regulation of networked control systems under finite bandwidth constraints and its applications, *IEEE Trans. Autom. Control*, **69** (2024), 6490–6497. https://doi.org/10.1109/TAC.2024.3388296
5. X. Wang, J. Zhang, C. Chen, J. He, Y. Ma, X. Guan, Trust-AoI-aware codesign of scheduling and control for edge-enabled IIoT systems, *IEEE Trans. Ind. Inf.*, **20** (2024), 2833–2842. https://doi.org/10.1109/TII.2023.3299040
6. Y. Ma, J. Guo, Y. Wang, A. Chakrabarty, H. Ahn, P. Orlik, et al., Optimal dynamic transmission scheduling for wireless networked control systems, *IEEE Trans. Control Syst. Technol.*, **30** (2022), 2360–2376. https://doi.org/10.1109/TCST.2022.3141581
7. M. Luan, Z. Chang, S. Mumtaz, G. Min, T. Hämäläinen, End-edge collaborative control for AoI-aware short-packet industrial cyber-physical system, *IEEE J. Sel. Areas Commun.*, **43** (2025), 3104–3117. https://doi.org/10.1109/JSAC.2025.3574617
8. L. Li, A. E. Kalør, P. Popovski, W. Chen, Unified timing analysis for closed-loop goal-oriented wireless communication, *IEEE Trans. Wireless Commun.*, **24** (2025), 2814–2831. https://doi.org/10.1109/TWC.2024.3525087

9. L. Chen, Y. Xu, M. Li, B. Hu, H. Guo, Z. Liu, Privacy-preserving lightweight time-series anomaly detection for resource-limited industrial IoT edge devices, *IEEE Trans. Ind. Inf.*, **21** (2025), 4435–4446. https://doi.org/10.1109/TII.2025.3538127
10. X. Fang, C. Lei, W. Feng, Y. Chen, M. Xiao, N. Ge, et al., Sensing-communication-computing-control closed-loop optimization for 6G digital twin-empowered robotic systems, *IEEE J. Sel. Areas Commun.*, **43** (2025), 3330–3346. https://doi.org/10.1109/JSAC.2025.3574601
11. P. Peng, W. Tao, H. Wang, H. Zhao, Intelligent perception communication protocol for satellite constellations via multi-agent deep reinforcement learning with dual-attention and delay-aware coordination, *Electron. Res. Arch.*, **34** (2026), 5546–5579. https://doi.org/10.3934/era.2026248
12. X. Zhu, X. Zhang, J. Wei, C. Wen, H. Lin, Periodic event-triggered quantized control for nonlinear systems with packet losses and large transmission delays, *IEEE Trans. Autom. Control*, **71** (2026), 3926–3941. https://doi.org/10.1109/TAC.2026.3653601
13. Y. Hu, O. M. Kwon, S. H. Lee, H_∞ control for interval type-2 fuzzy singularly perturbed systems with multi-node round-robin protocol and packet dropouts, *Fuzzy Sets Syst.*, **500** (2025), 109202. https://doi.org/10.1016/j.fss.2024.109202
14. J. Cheng, W. Wei, Y. Wang, M. V. Basin, D. Zhang, Random time-space sampled-data control of T-S fuzzy reaction-diffusion neural networks with time-delayed communication scheme, *IEEE Trans. Syst. Man Cybern. Syst.*, **55** (2025), 7964–7973. https://doi.org/10.1109/TSMC.2025.3598279
15. W. Wang, H. Zeng, J. Liang, S. Xiao, Sampled-data-based load frequency control for power systems considering time delays, *J. Franklin Inst.*, **362** (2025), 107477. https://doi.org/10.1016/j.jfranklin.2024.107477
16. W. Wang, J. Liang, H. Zeng, Sampled-data-based stability and stabilization of Lurie systems, *Appl. Math. Comput.*, **501** (2025), 129455. https://doi.org/10.1016/j.amc.2025.129455
17. H. Zeng, K. Teo, Y. He, W. Wang, Sampled-data-based dissipative control of T-S fuzzy systems, *Appl. Math. Model.*, **65** (2019), 415–427. https://doi.org/10.1016/j.apm.2018.08.012
18. Z. Zhang, Q. Liu, M. H. Mamduhi, S. Hirche, Average communication rate for networked event-triggered stochastic control systems, *IEEE Trans. Control Netw. Syst.*, **12** (2025), 1894–1905. https://doi.org/10.1109/TCNS.2025.3546788
19. H. Sun, H. Mu, J. Sun, H. Han, J. Qiao, Output feedback synthesis for networked control systems with packet dropouts and multiple probability sampling periods: The stochastic communication protocol case, *IEEE Trans. Cybern.*, **55** (2025), 4808–4819. https://doi.org/10.1109/TCYB.2025.3594482
20. Z. Lu, G. Guo, Control and communication scheduling co-design for networked control systems: A survey, *Int. J. Syst. Sci.*, **54** (2023), 189–203. https://doi.org/10.1080/00207721.2022.2097332
21. J. Zhou, D. Xu, W. Tai, C. K. Ahn, Switched event-triggered H_∞ security control for networked systems vulnerable to aperiodic DoS attacks, *IEEE Trans. Netw. Sci. Eng.*, **10** (2023), 2109–2123. https://doi.org/10.1109/TNSE.2023.3243095

22. M. Hao, G. Zhuang, G. Cui, J. Xia, Observer-based dynamic event-triggered finite-time switching control for networked discrete implicit DC circuit systems under aperiodic DoS attacks, *IEEE Trans. Autom. Sci. Eng.*, **22** (2025), 22925–22937. https://doi.org/10.1109/TASE.2025.3624969

23. Y. Yang, K. G. Vamvoudakis, H. Modares, Y. Yin, D. C. Wunsch, Safe intermittent reinforcement learning with static and dynamic event generators, *IEEE Trans. Neural Netw. Learn. Syst.*, **31** (2020), 5441–5455. https://doi.org/10.1109/TNNLS.2020.2967871

24. M. Shen, X. Wang, S. Zhu, Z. Wu, T. Huang, Data-driven event-triggered adaptive dynamic programming control for nonlinear systems with input saturation, *IEEE Trans. Cybern.*, **54** (2024), 1178–1188. https://doi.org/10.1109/TCYB.2023.3337779

25. Y. Yang, G. Liu, W. Xie, W. Zhang, Q. Li, C. K. Ahn, Asymptotic event-based tracking design for nonlinear systems under multiple unknown control directions, *IEEE Trans. Syst. Man Cybern. Syst.*, **55** (2025), 7604–7616. https://doi.org/10.1109/TSMC.2025.3595570

26. G. Zhuang, Y. Pang, G. Zong, J. Xia, NN-based dynamic adaptive triggered security compensation feedback control for implicit power systems subjected to FDI attacks, *IEEE Internet Things J.*, **12** (2025), 50493–50502. https://doi.org/10.1109/JIOT.2025.3609853

27. C. Jia, S. Sun, F. Han, X. Liu, Hybrid impulsive synchronization control of heterogeneous neural networks under dynamic and static event-triggered conditions, *Electron. Res. Arch.*, **34** (2026), 2607–2630. https://doi.org/10.3934/era.2026121

28. Y. Yang, L. Tang, W. Zou, J. Guo, C. K. Ahn, Dynamic event-triggered design with fixed-time performance and input dead-zone, *IEEE Trans. Circuits Syst. II Express Briefs*, **69** (2022), 4344–4348. https://doi.org/10.1109/TCSII.2022.3184734

29. H. Sun, C. Peng, X. Ge, Threshold-dependent secure event-triggered control for networked systems under denial of service attacks, *IEEE Trans. Autom. Sci. Eng.*, **22** (2025), 11139–11149. https://doi.org/10.1109/TASE.2025.3531944

30. C. Wu, X. Zhao, N. Zhao, N. Xu, Periodic and dynamic periodic event-triggered control for nonlinear cyber-physical systems under DoS attacks via a hybrid system approach, *IEEE Trans. Control Netw. Syst.*, **11** (2024), 221–232. https://doi.org/10.1109/TCNS.2023.3275918

31. H. Zeng, Z. Zhu, T. Peng, W. Wang, X. Zhang, Robust tracking control design for a class of nonlinear networked control systems considering bounded package dropouts and external disturbance, *IEEE Trans. Fuzzy Syst.*, **32** (2024), 3608–3617. https://doi.org/10.1109/TFUZZ.2024.3377799

32. W. Wang, J. Liang, H. Zeng, X. Zhang, Novel looped functionals in designing output feedback controllers for aperiodic sampled-data control systems, *IEEE Trans. Autom. Sci. Eng.*, **22** (2025), 16397–16402. https://doi.org/10.1109/TASE.2025.3573304

33. N. Lin, Q. Ling, Event-triggered quantized consensus of linear multiagent systems under asynchronous denial-of-service attacks, *IEEE Trans. Autom. Control*, **70** (2025), 697–704. https://doi.org/10.1109/TAC.2024.3422230

34. X. Kang, H. Ishii, W. P. M. H. Heemels, Resilient quantized control of uncertain networked systems under DoS attacks, *IEEE Trans. Control Netw. Syst.*, **13** (2026), 773–785. https://doi.org/10.1109/TCNS.2026.3662149

35. J. Xue, X. Ding, A. Slowik, H. Tong, Stabilization of sampled-data networked control systems under Markovian bit flips: an entropy-assisted predictive correction scheme, *IEEE Internet Things J.*, early access, **2026** (2026). https://doi.org/10.1109/JIOT.2026.3727448

36. N. Huo, D. Shen, D. Ho, Encoding–decoding-based quantized learning control using spherical polar coordinates, *IEEE Trans. Cybern.*, **55** (2025), 812–825. https://doi.org/10.1109/TCYB.2024.3496794

37. T. Liu, D. Shen, D. Ho, On general linear encoding–decoding pairs for quantized iterative learning control, *IEEE Trans. Cybern.*, **56** (2026), 2047–2060. https://doi.org/10.1109/TCYB.2025.3633720

38. Y. Liu, W. Yang, C. Su, Y. Luo, X. Wang, Observer-based control of networked periodic piecewise systems with encoding–decoding mechanism, *IEEE Trans. Cybern.*, **55** (2025), 2754–2764. https://doi.org/10.1109/TCYB.2025.3543878

39. M. Wakaiki, Stabilization of infinite-dimensional systems under quantization and packet loss, *IEEE Trans. Autom. Control*, **70** (2025), 6625–6640. https://doi.org/10.1109/TAC.2025.3564223

40. Y. Zhou, A. Polyakov, G. Zheng, Robust finite-time stabilization of linear systems with limited state quantization, *Automatica*, **171** (2025), 111967. https://doi.org/10.1016/j.automatica.2024.111967

41. J. Zhou, J. Dong, S. Xu, C. K. Ahn, Input-to-state stabilization for Markov jump systems with dynamic quantization and multimode injection attacks, *IEEE Trans. Syst. Man Cybern. Syst.*, **54** (2024), 2517–2529. https://doi.org/10.1109/TSMC.2023.3344869

42. M. Shen, C. Wang, Q. Wang, H. Yan, G. Zong, Z. Zhu, Fault-tolerant synchronization control of switched complex networks by a proportional-integral intermediate observer approach, *IEEE Trans. Cybern.*, **55** (2025), 4689–4698. https://doi.org/10.1109/TCYB.2025.3591393

43. H. Zeng, K. Teo, Y. He, A new looped-functional for stability analysis of sampled-data systems, *Automatica*, **82** (2017), 328–331. https://doi.org/10.1016/j.automatica.2017.04.051

44. M. Shen, C. Wang, Q. Wang, Y. Sun, G. Zong, Synchronization of fractional reaction-diffusion complex networks with unknown couplings, *IEEE Trans. Netw. Sci. Eng.*, **11** (2024), 4503–4512. https://doi.org/10.1109/TNSE.2024.3432997

45. Y. Yang, H. Modares, K. G. Vamvoudakis, F. L. Lewis, Composite adaptive critic design, *IEEE/CAA J. Autom. Sinica*, **12** (2025), 2525–2540. https://doi.org/10.1109/JAS.2025.125435

46. X. Li, H. Hong, S. Xiong, Y. Yu, Prescribed-time mean-square synchronization of stochastic coupled inertial neural networks with time delays via pinning control, *J. Nonlinear Dyn. Appl.*, **2** (2026), 61–75. https://doi.org/10.62762/JNDA.2026.284613



AIMS Press

© 2026 the Author(s), licensee AIMS Press. This is an open access article distributed under the terms of the Creative Commons Attribution License (http://creativecommons.org/licenses/by/4.0)